Progress in Aerospace Sciences 47 (2011) 217–239

Contents lists available at ScienceDirect

Progress in Aerospace Sciences

journal homepage: www.elsevier.com/locate/paerosci

Airship dynamics modeling: A literature review

Yuwen Li [a,*], Meyer Nahon [b], Inna Sharf [b]

[a] Department of Aerospace Engineering, Ryerson University, 350 Victoria Street, Toronto, Ontario, Canada M5B 2K3
[b] Department of Mechanical Engineering, McGill University, 817 Sherbrooke Street West, Montreal, Quebec, Canada H3A 2K6

ARTICLE INFO

Available online 14 December 2010

ABSTRACT

The resurgence of airships has created a need for dynamics models and simulation capabilities adapted to these lighter-than-air vehicles. However, the modeling techniques for airship dynamics have lagged behind and are less systematic than those for fixed-wing aircraft. A state-of-the-art literature review is presented on airship dynamics modeling, aiming to provide a comprehensive description of the main problems in this area and a useful source of references for researchers and engineers interested in modern airship applications. The references are categorized according to the major topics in this area: aerodynamics, flight dynamics, incorporation of structural flexibility, incorporation of atmospheric turbulence, and effects of ballonets. Relevant analytical, numerical, and semi-empirical techniques are discussed, with a particular focus on how the main differences between lighter-than-air and heavier-than-air aircraft have been addressed in the modeling. Directions are suggested for future research on each of these topics.

Contents

* Corresponding author.
E-mail addresses: yuwen.li@mail.mcgill.ca (Y. Li), Meyer.Nahon@mcgill.ca (M. Nahon), Inna.Sharf@mcgill.ca (I. Sharf).

0376-0421/$ - see front matter © 2010 Elsevier Ltd. All rights reserved.
doi:10.1016/j.paerosci.2010.10.001

1. Introduction

An airship is a lighter-than-air (LTA) aircraft equipped with propulsion and steering systems. Unlike conventional heavier-than-air (HTA) vehicles such as fixed-wing aircraft and helicopters, whose lift is aerodynamically generated by the motion of an airfoil through the air, airships stay aloft using a light lifting gas. This distinguishing feature can provide them with long endurance, high payload-to-weight ratio, and low fuel consumption.

Airships are the first aircraft that realized mankind's dream of controlled, powered flight. In 1784, Jean-Baptiste Meusnier proposed a design for an airship of ellipsoidal shape with a rudder, an elevator, and three large airscrews, but he lacked a lightweight, powerful engine. Henri Giffard was the first person to apply steam-engine technology successfully to airships. He flew his airship 17 miles in 1852, with a single propeller driven by a three horsepower engine [1]. The golden age of airships began with the launch of the Luftschiff Zeppelin LZ1 in 1900. The Zeppelin airships became the most famous aircraft of that time and some of these airships were used as bombers during World War I by the German Army. The United States and Britain built several airships, such as the R-33, R-34 British airships and the American USS Shenandoah (ZR-1), in the 1920s and 1930s, mostly imitating the original Zeppelin design. But the use of airships declined over time as fixed-wing aircraft became more capable and with the occurrence of several airship accidents, including the 1937 burning of the Hindenburg, the largest aircraft ever built. Although the use of airships has been in recession for decades, over the past few years, the advancement of modern techniques, such as composite materials, optimal design, computational fluid dynamics (CFD), thermal modeling, vectored thrust, and automatic control, have all brought a resurgence of these aircraft [2,3]. A wide range of applications have recently been proposed for modern airships in commercial, scientific, and military fields, such as advertising and tourism [4], surveillance [5], environmental monitoring [6–8], planetary exploration [9,10], heavy-lift cargo transport [11], and stratospheric observation and telecommunication relay [12–14].

All of the aforementioned airship applications require a common design tool: dynamics modeling and simulation, to analyze their flight behavior, design their control systems, and optimize their flight trajectories. The dynamics modeling of conventional HTA aircraft has been broadly studied and has become highly reliable. However, for a variety of reasons, limitations exist when applying these HTA dynamics models, such as those developed by Etkin [15], to airships. First, an airships' lift generation mechanism is different from that of HTA aircraft due to the use of light lifting gas. Certain solid–fluid interaction forces can be neglected for HTA aircraft, such as buoyancy and those related to the inertia of the surrounding air, but these forces become important for airships. Second, airships have very different shape and structure compared with HTA aircraft. For example, many modern airships have ballonets—components to LTA aircraft that can influence their dynamics characteristics. Third, the HTA dynamics models are highly reliable for airplanes because of well-developed analytical and numerical techniques and a great deal of constantly updated empirical data. But the dynamics modeling techniques and relevant experimental studies for airships have lagged behind and are less systematic than those for airplanes.

Existing works on airship dynamics are scattered over a range of journals, books, and technical reports, and a large number of conference proceedings. These articles have been published over a period of many decades, witnessing the ascent, golden age, decline, and recent resurgence of airships. In 1999, Khoury and Gillett edited an important book [3] for use as a guide to the development of modern airships. The book addresses a wide range of issues including airship design, dynamics, control, propulsion, and piloting. Significant progress has been made in the area of airship dynamics since then. Many new modeling techniques and important issues in airship dynamics are not covered in Khoury and Gillett's text, such as recent CFD methods to analyze airship aerodynamics, fluid–structure interaction in airships, the incorporation of atmospheric turbulence, and the effects of ballonets on airship dynamics. In 2009, Liao and Pasternak [16] published a literature review of unconventional hull designs and airship structural analysis. However, their review is focused on airship designs and materials but has little information on the dynamics characteristics.

To meet the requirements of modeling and simulation for the resurgence of airships, a state-of-the-art literature review focusing on airship dynamics is presented. This article aims to provide a comprehensive description of the main problems in airship dynamics modeling and summarize the theoretical (analytical or numerical) and semi-empirical techniques to solve these problems.

Five topics are discussed in this article: aerodynamics, flight dynamics, incorporation of structural flexibility, incorporation of atmospheric turbulence, and effects of ballonets. These topics cover most of the problems and modeling techniques in airship dynamics reported in literature. Aerodynamics and flight dynamics are fundamental issues in airship design, which have been investigated over many decades. In Sections 2 and 3, we first review the aerodynamics and flight dynamics models of airships that are based on a rigid-body assumption. Structural strength was a significant issue in the development of old airships. However, the influence of structural flexibility on airship aerodynamics and flight dynamics has been investigated only in the past few years because of the recent advances in computational capabilities. The fluid–structure interaction in airships is discussed in Section 4. Researchers have realized for a long time that airships' flight characteristics are vulnerable to wind and gusts. However, incorporating atmospheric turbulence into the mathematical dynamics models of airships is not straightforward and differs from the methodologies for HTA aircraft due to the existence of light lifting

Nomenclature

$\mathbf{A}$, $\mathbf{B}$	state matrix and input matrix of the linear model
C_{DC}	hull cross-flow drag coefficient
C_{D0}	hull axial drag coefficient
$C_{L\alpha}$	lift curve slope
C_F	skin-friction coefficient of an equivalent flat plate
$\mathbf{C}_{wb}$	rotation matrix from the wind-axes frame to the body frame
D	drag force
D_m	maximum diameter of the hull
$\mathbf{F}_A$, $\mathbf{M}_A$	added-mass force and moment
$\mathbf{F}_{AD}$, $\mathbf{M}_{AD}$	aerodynamic force and moment
$\mathbf{F}_C$, $\mathbf{M}_C$	control force and moment
$\mathbf{F}_f$, $\mathbf{M}_f$	force and moment due to flow motion
F_N, M_N	aerodynamic normal force and pitch moment
$\mathbf{g}$	acceleration of gravity
H	altitude of the airship
h_1	vertical position of m_1 from the ballonet CG, see Fig. 20(a)
I	second moment of area of the hull's cross-section
$\mathbf{J}$	inertia tensor of the airship
k_1, k_2, k'	added-mass factors, see Fig. 4
L_a	length of the airship
l_h	distance from the nose to the hull–fin intersection point
l_{zb}, l_{zg}	vertical distances from the hull CV to the CGs of the ballonet air and lifting gas
M	bending moment
$\hat{M}$, $\hat{C}$, $\hat{K}$	equivalent mass, damping coefficient, and stiffness of the ballonet sloshing model in Eq. (33)
$\mathbf{M}_{AA}$	added-mass matrix of the airship
m	total mass of the airship
m', J'	mass and moment of inertia of the displaced air
m_b, m_g	masses of ballonet air and lifting gas
m_{b0}, I_{b0}	mass and moment of inertia of the ballonet air that does not move relative to the hull, see Fig. 20(a)
m_{Fij}	added-mass terms due to the fins
m_i	sloshing masses of ballonet air, see Fig. 20(a)
p	internal pressure
Q	shear force
q_{ei}	generalized elastic coordinates
q_0	dynamic pressure
R,S	hull cross-sectional radius and area
Re	Reynolds number
R_T	turn radius
$\mathbf{r}_G$, $\mathbf{r}_V$, $\mathbf{r}_{bk}$	position vectors of CG, CV, and ballonets from the body-frame origin
u_0	equilibrium forward speed
V_B, V_b, V_g	airship volume, ballonet volume, and lifting gas volume
$\mathbf{v}=[u,v,w]^{\mathrm{T}}$	linear velocity
$\mathbf{v}_f=[u_f,v_f,w_f]^{\mathrm{T}}$	flow velocity at the location of the body-frame origin
$\mathbf{v}_g$, $\mathbf{v}_w$	gust speed and mean wind speed
$\mathbf{x}$, $\mathbf{u}$	deviation of state and control vectors from equilibrium condition
y_1	displacement of m_1, see Fig. 20(a)
α	angle of attack of the airship
α_g	gust angle of attack
β	sideslip angle
ε	longitudinal distance from the nose
ε_v	longitudinal position at which the flow ceases to be potential
η	efficiency factor for the cross-flow drag due to finite length
η_k, η_F	hull–fin influence factors in Eq. (7)
λ	equivalent distance from the CV to the point at which the total side force acts
Ω	wave number
$\boldsymbol{\omega}=[p,q,r]^{\mathrm{T}}$	angular velocity
ω_1, ζ_1	undamped natural frequency and damping ratio of m_1, see Fig. 20(a)
$\mathbf{\Phi}_{ei}$	shape functions
$\mathbf{\Phi}_v$	spatial gradient matrix of non-uniform flow velocity, see Eq. (22)
ϕ, θ	roll and pitch angles
ρ	air density
σ_L, σ_H	longitudinal and hoop membrane stresses of the hull envelope
θ_w	wrinkling angle of the hull envelope

gas. Important works on this topic have been published in the past decade, which are reviewed in Section 5. Ballonets are used for the control of internal pressure in modern LTA aircraft. Considering that the ballonets can occupy a large volume and can slosh within the airship, researchers have been interested in the influence of ballonets on the flight of LTA aircraft. This topic is particular to airship dynamics and does not appear in HTA dynamics modeling. Relevant modeling methods are discussed in Section 6. In addition, relevant wind-tunnel and other experimental data for airships are also summarized in the corresponding sections of this article.

2. Aerodynamics

A typical airship has a large streamlined hull filled with a light gas, actuated by thrusters and equipped with controllable low-aspect-ratio tail fins, as shown in Fig. 1. The thrusters, sometimes vectorable, are usually installed on a gondola, although a thruster is sometimes installed on the downward vertical fin to provide additional yaw control.

The flight behavior of an airship depends upon the interaction forces between the aircraft and the air, which include aerostatics and aerodynamics. The former is due to the static air pressure and is independent of the motion of the vehicle, while the latter is related to its motion. Most of the lift on the airship is due to aerostatics. However, since the aerostatics is fairly simple to derive [17], the aerodynamic computation becomes the more important issue in airship dynamics analysis.

2.1. Wind-tunnel tests

Before we proceed to discuss computational aerodynamic methods for airships, we first revisit some important wind-tunnel test results of these aircraft, from which we deduce the main issues in their aerodynamics modeling.

Wind-tunnel tests have been critical to airship dynamics analysis, especially in the golden age of airships when no accurate aerodynamics models were available. Two review papers on airship wind-tunnel tests can be found in literature: by Jones [18] who summarized the aerodynamic characteristics of several British airships from experiments in the 1910s and 1920s, and by Curtiss [19] which is a review paper on LTA aerodynamic experiments up to 1976. Much wind-tunnel data on scaled airship models was

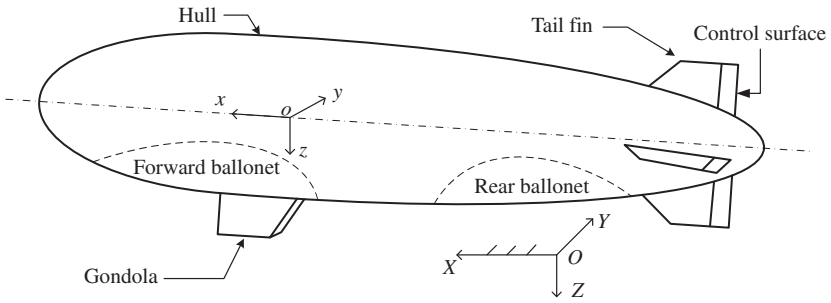

Fig. 1. A typical airship.

Table 1
Available wind-tunnel data for some airships.

LTA model	Aerodynamics results		
	Steady-state	Pressure distribution	Rotational derivatives
Akron [20,21]	✓	✓	
Shenandoah [22]	✓		✓
R-101 [23,24]	✓	✓	✓
YEZ-2A [25]	✓		✓
Lotte [26]	✓	✓	
TCOM-250 [27]			✓

collected decades ago in the reports of the National Advisory Committee for Aeronautics (NACA) in the United States and the Aeronautical Research Council (ARC) in Britain, in particular, for models of the American Akron (ZRS-4) [20,21], Shenandoah (ZR-1) [22], and the British R-101 [23,24] airships. Nowadays, wind-tunnel tests are still an important means to facilitating the development of modern airships and other LTA vehicles, such as the YEZ-2A [25] and Lotte [26] airships and the TCOM-250 aerostat [27]. These wind-tunnel results include steady-state aerodynamic coefficients, pressure distributions, and rotational stability derivatives, as listed in Table 1.

The following observations can be made from airship wind-tunnel tests, which also reveal the main issues in airship aerodynamics modeling:

- The hull of an airship experiences a nose-up pitch moment at non-zero angles of attack. This can be illustrated by the normal aerodynamic force distribution on the bare hull of the Akron model at an angle of attack of 12° in Fig. 2, where F_N is the aerodynamic force normal to the hull's centerline and ε denotes the longitudinal position from the nose, and the normal force per unit length is normalized by the dynamic pressure q_0. The normal force distribution at the front and at the rear both contributes to this nose-up aerodynamic moment. This aerodynamic moment is unstable because it increases as the angle of attack increases, as shown by the pitch moment coefficients of the bare hull of the Akron model in Fig. 3(b). The pitch moment M_N is taken about the center of volume (CV) of the airship and is normalized by q_0 and the airship volume V_B. This phenomenon of unstable pitch moment can be explained using potential flow theory which we will discuss in Section 2.2.
- Potential flow theory cannot fully capture the real aerodynamics of the bare hull because of the effects of viscosity, especially at the rear of the body. When the angle of attack is close to 0°, the flow is axial and mostly remains attached to the hull. As the angle of attack increases, flow separates at the rear, and vortex pairs are shed behind the hull. At an angle of attack of 90°, cross flow over the hull is dominant, similar to a cylinder placed normal to an oncoming flow. Existing methods to account for the viscous effects will be summarized in Section 2.3.
- The tail fins, not only produce extra lift force, but also provide a stabilizing effect on the airship against the aforementioned unstable pitch moment. This can be observed by comparing the normal force and pitch moment coefficients of a bare hull to those of the whole airship (hull plus fins), such as those plotted in Fig. 3 for the Akron model. Exploiting the similarities between fins and wings, the aerodynamic force on a pair of fins joined together (without the hull) can be predicted using low-aspect-ratio wing theories, such as those in [28], and will not be repeated here. The hull–fin interaction plays an important role on airship aerodynamics. Curtiss [19] uncovered from the data obtained on the R-101 and Akron models that the two fins directly joined together produced about 30–40% less lift than the two fins separated by the hull. In addition, the hull equipped with fins also produces more lift than a bare hull, as demonstrated in the force distribution at the rear of the hull for the two cases in Fig. 2. The incorporation of hull–fin interaction into the aerodynamic computation will be discussed in Section 2.4.
- The hull is the main source of the drag on an airship. On most airships, between 50% and 75% of the total drag is contributed by the hull [19], and the tail fins' drag is about 7–27% of the hull drag [3]. Drag prediction methods for airship hulls will be reviewed in Section 2.5.

2.2. Potential flow aerodynamics

The aerodynamic characteristics of airships were initially investigated in the 1920s, and many theoretical works on the aerodynamics of old airships are based on potential flow theory. An important example is the report by Munk [29], in which a slender body assumption is applied to derive the aerodynamic normal force per unit length along the hull at an angle of attack α as follows:

$$\frac{dF_N}{d\varepsilon} = (k_2 - k_1) q_0 \frac{dS}{d\varepsilon} \sin 2\alpha \tag{1}$$

where S is the local cross-sectional area of the hull. The factor $(k_2 - k_1)$ accounts for the finite length of hull, where k_1 and k_2 are the added-mass factors of ellipsoids in the longitudinal and lateral directions, respectively, derived by Lamb [30]. These are plotted as functions of D_m/L_a in Fig. 4 in which D_m is the maximum cross-sectional diameter of the hull and L_a is the length of the airship [31]. The resulting force distribution at the front of the hull reasonably matches the wind-tunnel data (see Fig. 2). The normal force and pitch moment can be obtained by integrating the force distribution over the hull. The normal force result obtained by integrating Eq. (1) is zero, because the hull has a closed planform. The resulting pitch moment reveals that at non-zero angles of attack, the hull experiences an unstable pitch moment, which was also observed

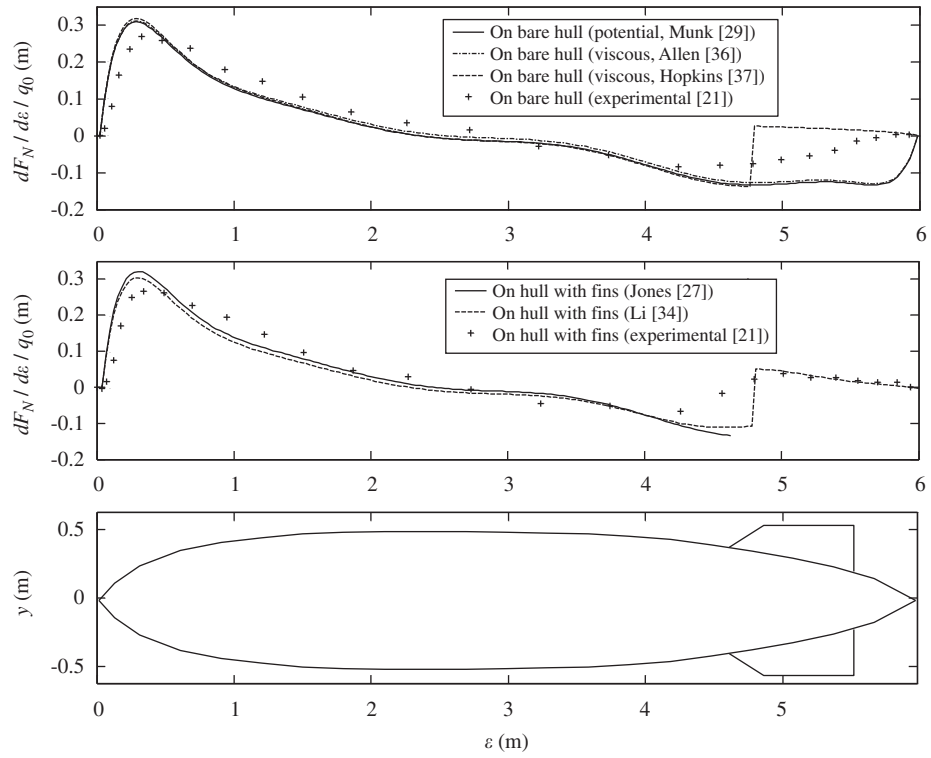

Fig. 2. Normal force per unit length on the hull of the Akron model at an angle of attack of 12°.

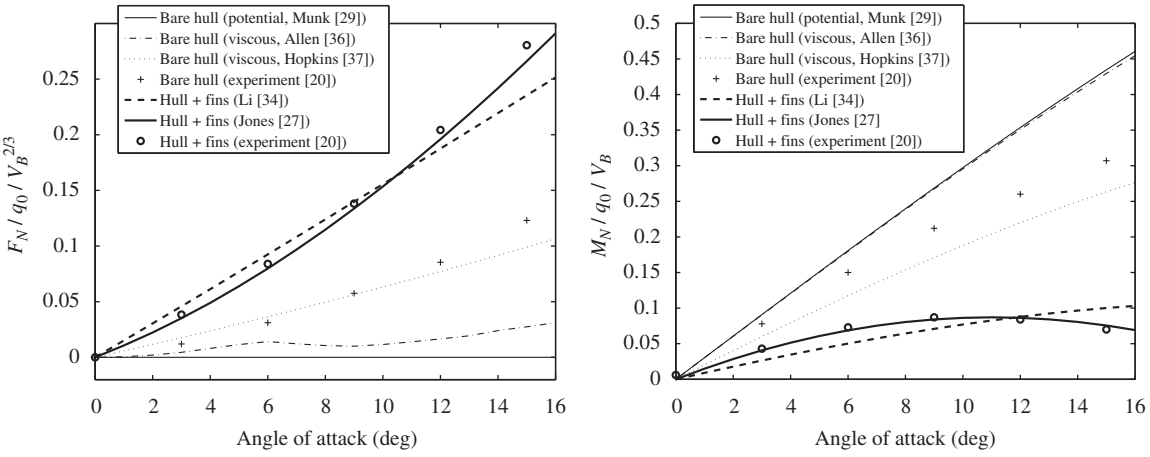

Fig. 3. Normal force and pitch moment coefficients of the Akron model.

from the wind-tunnel tests. Similarly, at non-zero sideslip angles, the hull experiences an unstable yaw moment.

Eq. (1) can be used to calculate the aerodynamic force and moment on a vehicle moving in a potential fluid with steady translation. A complete formulation of potential flow aerodynamics of a 6-DOF vehicle moving in an unbounded heavy fluid has been developed in the field of hydrodynamics for submarines and underwater vehicles. The potential fluid is governed by the Laplace equation with the boundary condition that the fluid remains attached to the body surface, and then the aerodynamic force can be derived via Kirchhoff's equation [30,17] or Bernoulli's equation [31]. Kirchhoff's equation gives the total forces and moments on the vehicle from the kinetic energy of the fluid, while Bernoulli's equation not only provides these quantities but also can be used to calculate the pressure distribution over the vehicle. The resulting aerodynamic loading is usually called the *added-mass force and moment*, and it can be summarized in vector form as [17]

$$\begin{bmatrix}\mathbf{F}_A\\ \mathbf{M}_A\end{bmatrix} = -\begin{bmatrix}\mathbf{M}_{11} & \mathbf{M}_{12}\\ \mathbf{M}_{21} & \mathbf{M}_{22}\end{bmatrix}\begin{bmatrix}\dot{\mathbf{v}}\\ \dot{\boldsymbol{\omega}}\end{bmatrix} - \begin{bmatrix}\boldsymbol{\omega}^{\times}(\mathbf{M}_{11}\mathbf{v}+\mathbf{M}_{12}\boldsymbol{\omega})\\ \mathbf{v}^{\times}(\mathbf{M}_{11}\mathbf{v}+\mathbf{M}_{12}\boldsymbol{\omega})+\boldsymbol{\omega}^{\times}(\mathbf{M}_{21}\mathbf{v}+\mathbf{M}_{22}\boldsymbol{\omega})\end{bmatrix} \tag{2}$$

where $\mathbf{v}=[u,v,w]^{\mathrm{T}}$ and $\boldsymbol{\omega}=[p,q,r]^{\mathrm{T}}$ denote the 3×1 linear and angular velocity vectors of the vehicle expressed in a reference frame fixed to it, respectively. The coefficient matrix in the first term on the right hand side is the 6×6 symmetric added-mass matrix. The first term in Eq. (2) is related to the time rates of change of the linear and angular velocities of the vehicle, while the second is related to the coupling of the linear and angular velocities. In particular, for a vehicle in steady translation ($\dot{\mathbf{v}}=\dot{\boldsymbol{\omega}}=\boldsymbol{\omega}=\mathbf{0}$), only

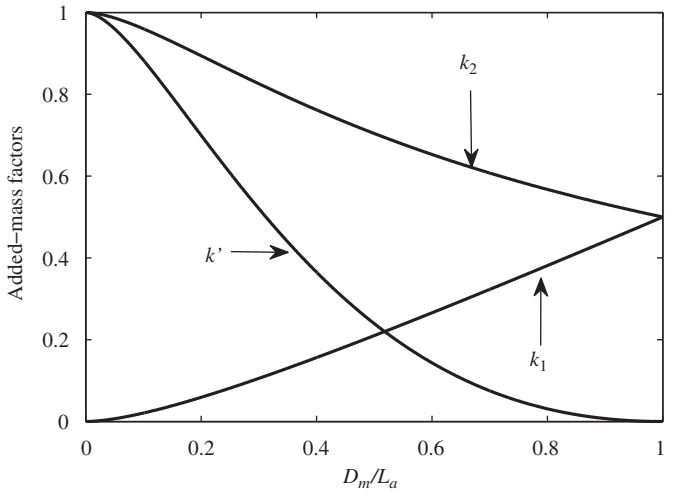

Fig. 4. Added-mass factors [31].

the moment term $-\mathbf{v}^{\times}(\mathbf{M}_{11}\mathbf{v})$ appears in Eq. (2), which is the aforementioned "Munk moment" as it can be derived from Munk's equation (1).

To evaluate the potential flow aerodynamics with Eq. (2), the added-mass matrix must be computed. For a body of irregular shape, the added-mass matrix can be obtained using numerical approaches [32]. The exact solution for the added-mass matrix of some regular shapes can be found in [33]. In particular, the results for ellipsoids [30] have been commonly used to evaluate the added-mass matrices of airship hulls. If the body-fixed frame is at the CV of an airship, with the x axis along the centerline and pointing to the nose, the z axis positively downward, and the positive y axis determined by the right hand rule, the added-mass matrix of an airship with the shape in Fig. 1 can be written as

$$\mathbf{M}_{AA}=\begin{bmatrix} k_1m' & 0 & 0 & 0 & 0 & 0 \\ & k_2m'+m_{F22} & 0 & 0 & 0 & m_{F26} \\ & & k_2m'+m_{F33} & 0 & m_{F35} & 0 \\ & & & m_{F44} & 0 & 0 \\ & \text{symmetric} & & & k'J'+m_{F55} & 0 \\ & & & & & k'J'+m_{F66} \end{bmatrix} \tag{3}$$

where k_1m', k_2m', and $k'J'$ in the diagonal terms are due to the hull, and the other terms are due to the fins (denoted by subscript F). The added-mass factors k_1, k_2, and k' are plotted as functions of D_m/L_a in Fig. 4, and m' and J' are the mass and the moment of inertia of the air displaced by the hull, respectively. The tail fins should be considered in the calculation of added-mass matrix of an airship, because they can contribute close to 40% of the total added moments of inertia through the terms m_{F55} and m_{F66} [32,34]. Readers are referred to [34,33] for prediction methods to determine the added-mass terms of the fins.

The added-mass matrix in Eq. (3) is given in a specific body frame. If the body frame is located at a different position or with different orientation, the added-mass matrix can be obtained through a transformation derived from the invariance of the kinetic energy of the fluid [35]. To be consistent with the added-mass aerodynamics, we also express other aerodynamic forces in the body-fixed frame in Sections 2.3– 2.5.

2.3. Viscous effect on hull

Semi-empirical methods are still used to account for the effect of viscosity in the computation of normal force on the airship hull due to their simple formulations. To correct the normal force calculation for the influence of viscosity for an inclined body of revolution, Allen [36] assumed that the viscous contribution at each station on the local cross section is equal to the steady-state drag on a section of an infinite-length circular cylinder placed normal to the flow. By adding a term related to this cross-flow drag to Munk's equation (1), the normal force per unit length along the hull is computed as [36]

$$\frac{dF_N}{d\varepsilon}=(k_2-k_1)q_0\frac{dS}{d\varepsilon}\sin 2\alpha\cos\frac{\alpha}{2}+2q_0R\eta C_{DC}\sin^2\alpha \tag{4}$$

where C_{DC} is the cross-flow drag coefficient of an infinite-length circular cylinder, η is an efficiency factor accounting for the finite length of the body and determined from its fineness ratio, R is the local cross-sectional radius. The first term on the right hand side of Eq. (4) comes from Eq. (1). The multiplication by $\cos(\alpha/2)$ is introduced because this force is directed midway between the normal to the body centerline and the normal to the wind direction, as pointed out in [36]. As plotted in Fig. 2, the difference in the normal force per unit length between Munk's equation (1) and Allen's equation (4) is relatively small for the hull of the Akron model.

In a similar semi-empirical method by Hopkins [37], it is assumed that the aerodynamic normal force on the front portion of the body can be calculated using a potential flow assumption (i.e., Eq. (1)) while the force on the remaining portion is due to the cross-flow drag. Using this approach, the normal force distribution on a body of revolution at low angles of attack can be obtained as [37]

$$\frac{dF_N}{d\varepsilon}=\begin{cases} 2(k_2-k_1)q_0\alpha\frac{dS}{d\varepsilon} & \text{if } 0\le\varepsilon\le\varepsilon_v \\ 2q_0R\eta C_{DC}\alpha^2 & \text{if } \varepsilon_v<\varepsilon\le L_a \end{cases} \tag{5}$$

where ε_v is the position at which the flow ceases to be potential. Hopkins' model requires the estimation of ε_v, which is empirically determined from wind-tunnel test results as [37]

$$\varepsilon_v=0.378L_a+0.527\varepsilon_1 \tag{6}$$

where ε_1 denotes the position at which $dS/d\varepsilon$ has a maximum negative value.

Besides separating the region where the viscous effect acts and the small angle approximation made in Eq. (5), Hopkin's and Allen's methods are also different in the calculation of the cross-flow drag coefficient C_{DC}. In Hopkin's method [37,38], C_{DC} is assumed to have a constant value of 1.2, while in Allen's method [36], it varies between 0.3 and 1.2. These differences cause different normal force results from the two methods.

The normal force distribution and resulting normal force and pitch moment for the Akron model's bare hull from these two methods are compared to wind-tunnel data in Figs. 2 and 3. Note that the force per unit length obtained from Eq. (5) is discontinuous at ε_v. As illustrated in Fig. 3, the force and moment from Eq. (5) are in better agreement with experiment than Eq. (4) for airship hulls at low angles of attack. The results from Eq. (5) were validated with wind-tunnel tests on a series of hull-shaped bodies at angles of attack up to 20°, while Eq. (4) was validated for long space-shuttle-like bodies with a blunt base. However, Eq. (4) has the advantage that it can be easily extended to the full range of angle of attack from 0° to 180° [39,40]. This extension to high angles of attack is problematic for Eq. (5) due to the absence of wind-tunnel data from which to obtain ε_v at high angles of attack.

Eqs. (4) and (5) include both the potential flow and viscous terms, while the potential flow aerodynamics is also incorporated in Eq. (2). Thus, care should be taken not to overcount the potential flow aerodynamics when combining Eqs. (2) and (4) or (5) in the aerodynamic calculation. For example, if Eq. (4) or (5) is used for the steady-state pitch moment calculation, the term $-\mathbf{v}^{\times}(\mathbf{M}_{11}\mathbf{v})$ should be dropped from Eq. (2).

2.4. Hull–fin interaction

The hull–fin interaction, as observed in wind-tunnel tests, was difficult to estimate in the early years of airship development. Prediction methods for hull–fin interaction were later investigated for missiles and airplanes, for example, by Pitts et al. [41]. However, these methods were not applied to airships because their development had declined by that time.

In the 1980s, Jones and DeLaurier [27] proposed a semi-empirical approach to predict the steady-state aerodynamics of aerostats[1] and airships, with a particular focus on the hull–fin interaction. In their steady-state model, an airship is divided into two distinct aerodynamic regions: the hull, extending from the nose to the hull–fin intersection point, and the fins, from that point to their trailing edge. The total aerodynamic force is obtained by adding the contributions of the two regions. For example, the normal force on an airship at an angle of attack α is computed as [27]

$$F_N = (k_2-k_1)\eta_k q_0 \sin 2\alpha \cos\frac{\alpha}{2}\int_0^{l_h}\frac{dS}{d\varepsilon}\,d\varepsilon + q_0 C_{DC}\sin\alpha\sin|\alpha|\int_0^{l_h}2R\,d\varepsilon + q_0 S_F C_{n\alpha F}\eta_F\frac{\sin 2\alpha}{2} + q_0 S_F C_{DCF}\sin\alpha\sin|\alpha| \quad (7)$$

where l_h is the distance from the nose to the hull–fin intersection point, S_F and C_{DCF} are the reference area and cross-flow drag coefficient of the fins, respectively, and $C_{n\alpha F}$ is the derivative of normal force of the fins with respect to α. The normal aerodynamic loads on the hull (the first two terms in Eq. (7)) are modeled as distributed forces in a similar way to Eq. (4), but with a hull–fin influence factor η_k in the first term and without the efficiency factor η in the second term. As well, writing $\sin\alpha\sin|\alpha|$ instead of $\sin^2\alpha$ in Eq. (7) allows us to deal with negative angles of attack. The loads on the fins are modeled as two point forces (the last two terms in Eq. (7)): one at the center of pressure and the other at the center of area. The influence factors η_k and η_F are introduced to account for the interaction between the hull and the fins; these factors are estimated from wind-tunnel test results.

In the aerodynamic computational approach by Li and Nahon [34], the hull–fin interaction is incorporated analytically. First, the effect of fins on the hull force is taken into account by adding a term due to the fin-induced downwash. Second, the influence of the hull on the fins is taken into account by using an effective local angle of attack to calculate the fins' forces, i.e.,

$$\alpha_e = \left(1+\frac{R^2}{s^2}\right)\alpha_F \quad (8)$$

where s is spanwise distance from the airship centerline and α_F is the local geometric angle of attack of the fin. The factor $(1+R^2/s^2)$ accounts for the influence of the hull [41]. Using the value of $(1+R^2/s^2)$ at the center of 1/4-chord, the geometric angle of attack α_f (representing the lift on two fins directly joined together) is lower than the effective one α_e (representing the lift on two fins mounted on a hull) by approximately 36% for the Akron airship, which is in agreement with the wind-tunnel test result discussed in Section 2.1.

The normal force distribution and the resulting normal force and pitch moment are computed for the Akron model using the methods in [27,34] to account for the hull–fin interaction and are shown in Figs. 2 and 3. Li and Nahon's method [34] provides more detail on the force distribution at the rear of the hull (see the second plot in Fig. 2), since Jones and DeLaurier's method [27] assumes that the aerodynamics after the hull–fin intersection point can be modeled with two point forces. It is not surprising that Jones and DeLaurier's model leads to more accurate force and moment results (see Fig. 3), because the wind-tunnel data of the Akron model were used to obtain the hull–fin influence factors η_k and η_F in their model.

The extension of steady-state aerodynamic model to an airship in general rigid-body motion (translation plus rotation) is also discussed in [27,34]. This issue is important for the simulation of airships in curvilinear flight. The formulation for the added-mass terms in Eq. (2) is, in fact, for general rigid-body motion, but the viscous effects in Eqs. (4) and (5) and the force in Eq. (7) presume steady translation. To extend the steady-state aerodynamics, Jones and DeLaurier [27] discretized the airship into slices and used local accelerations and velocities to calculate the aerodynamic force and moment on different slices. They demonstrated that the trend of the calculated rotational aerodynamic derivatives for the TCOM 250 aerostat is in agreement with wind-tunnel measurements. It should be noted that in their slice model, the aerodynamics related to acceleration is considered, i.e., the added-mass terms are incorporated. In Li and Nahon's paper [34], Eqs. (2) and (5), the fin forces, and the hull–fin interaction effects are unified. To account for the rotation of the airship, the local velocities at ε_v are used to calculate the viscous effect and the local velocities at the centers of fins' 1/4-chords are used for fin force calculation. They implemented their aerodynamics computational approach in the flight simulation of the Skyship-500 airship. Simulation results of time responses to control surface deflections and steady turn rates match published flight test data [34].

2.5. Axial drag

Axial drag is of primary importance for computing required propulsive power and fuel consumption for airships. Wind-tunnel data shows that the hull is the main source of drag. A popular empirical method to predict the drag coefficient of a hull as a function of fineness ratio L_a/D_m is presented by Hoerner [44] as follows:

$$C_{D0} = C_F\left[4\left(\frac{L_a}{D_m}\right)^{1/3} + 6\left(\frac{L_a}{D_m}\right)^{-1.2} + 24\left(\frac{L_a}{D_m}\right)^{-2.7}\right] \quad (9)$$

where C_{D0} is the hull's axial drag coefficient non-dimensionalized by $V_B^{2/3}$ in which V_B is the body volume, C_F is the skin-friction coefficient of an equivalent flat plate and can be approximately computed as $C_F = 0.045Re^{-1/6}$ in which Re is the Reynolds number based on the hull length L_a. From Eq. (9), the minimum hull drag (about 8 C_F) occurs when the fineness ratio $L_a/D_m = 4.65$ in accordance with the prevailing airship designs, but the change in C_{D0} is small in the region close to this minimum value. The drag coefficient rises by only 10% as the values of L_a/D_m decreases from 4.65 to 2.8 and an even smaller drag rise is incurred for higher values of L_a/D_m up to 8 [45]. The optimization of hull shape usually requires more accurate drag calculation using CFD techniques, which will be discussed in the next subsection. Readers are referred to [3,45] for more information about the drag of other components of an airship and the drag of a spheroid-cone shaped airship.

2.6. CFD results

Recently, with the development of powerful computers, CFD techniques have been applied to analyze the aerodynamic characteristics of airships. An important example is the CFD packages developed by Lutz et al. for the Lotte airship [32]. Their codes couple panel methods with integral boundary-layer procedures to solve the Reynolds averaged Navier–Stokes equation [32,46].

[1] Some references on tethered aerostats are included in this review, because they are also streamlined LTA aircraft. The incorporation of tether dynamics is beyond the scope of this article and more information can be found in [42,43].

The inviscid velocity distribution resulting from the panel-method is used as input to the boundary-layer calculation with a 3D integration procedure. The shear-layer separation line on the body surface is obtained from the boundary-layer calculation and then used to improve the panel calculation by taking into account the wake influence due to the shear-layer separation. This cycle continues until a convergence of the separation line location. Lutz et al. used their codes to investigate the steady-state aerodynamic coefficients [47], added mass and moment of inertia [32], location of separation line of the hull [46,48], and propeller influence [49,50] for the Lotte airship.

CFD techniques are also used in the design of airships, in particular, for hull shape optimization. Lutz and Wagner [51] and Nejati and Matsuuchi [52] developed numerical tools for the optimization of airship hull shapes at zero angle of attack, with an objective to minimize the drag on a hull envelope of a given volume for a prescribed speed range. In both works, the panel codes are coupled with an integral boundary-layer procedure to account for the viscous effect. A source distribution on the body axis is chosen to model the body profile and the source strengths are used as design variables for the optimization process. The main difference between the techniques in [51,52] is in the calculation of transition region. In particular, Lutz and Wagner [51] used a semi-empirical criterion to determine the transition region, while in Nejati and Matsuuchi's method [52], the transition region is considered as a point at 3% of the body length. The results in both [51,52] show that the optimal hull shape and the resulting optimal drag coefficient vary depending on the Reynolds number regimes. To reduce the number of design parameters for hull optimization, Wang and Shan [53] expressed the hull profile as piecewise polynomials using eight parameters. In their panel method, the inviscid flow is computed from a distribution of sources on the airship surface, which provides the pressure and velocity at the body surface. The boundary layer is computed using an integral formulation of thin boundary-layer theory, and a semi-empirical method is used to locate the transition region. Commercial CFD packages have also been used to calculate the drag of a hull. Kale et al. [54] used FLUENT ™ to obtain the drag force for a multi-objective optimization of aerostat hulls. They defined a generic envelope hull profile in terms of a combination of two cubic-splines, with a spherical cap in the front portion, and a parabolic shape at the rear. The drag of the hull was reduced by 15.8% through their optimization.

Compared with the analytical or semi-empirical aerodynamic models in Sections 2.2–2.4, CFD packages can provide more detailed information, such as the pressure distribution and the location of the separation line, but incur much higher computational costs. The paper by Wong et al. [55] implies that simple computational expressions for airship aerodynamics can be obtained based on CFD results. They used source panels to model the hull and vortex-lattice panels for the fins to calculate the aerodynamic force and moment for several airships. It is demonstrated that the hull–fin influence factors η_k and η_f in Eq. (7) can be obtained from the CFD results. As can be seen in Fig. 5, the trends exhibited by these factors from CFD results [55] are similar to those from wind-tunnel data [27].

Finally, it is noted that coupling CFD and FEA (finite element analysis) codes is a viable approach to the aeroelastic analysis of airships and such works will be reviewed in Section 4.

2.7. Summary

Depending on the analysis objectives, one requires different information from the aerodynamic computation. A flight dynamics simulation based on a 6-DOF rigid-body model requires the total aerodynamic force and moment on the vehicle. On the other hand, an analysis which takes into account the structural flexibility effects (such as membrane wrinkling and fluid–structure interaction) requires force distribution or even pressure distribution to calculate the deformation. Correspondingly, airship aerodynamics models can be classified into the following three categories:

Total force/moment: The methods described in Sections 2.2– 2.5, either theoretical (such as Eqs. (1) and (2)) or semi-empirical (such as (4), (5) and (7)), can be used to calculate the total aerodynamic force and moment for the bare hull or the hull–fin combination. Notably, Eqs. (5) and (7) and the method in [34] have been validated using airship wind-tunnel or flight test data.

Force distribution: Eqs. (1), (4), (5), and (7), and the method in [34] all provide normal force per unit length. It should be noted that all these formulations give similar and reasonable force distribution predictions on the front part of the airship. However, the aerodynamic effects at the rear are much more complicated and accurate force distribution is still difficult to predict with these methods.

Pressure distribution: The methods in Sections 2.2– 2.5 cannot provide the pressure distribution on the airship envelope. Readers are referred to [30,31] for the pressure distribution on an ellipsoid moving in a potential fluid, which can be obtained from the analytical solution of the Laplace equation in terms of ellipsoidal harmonics. CFD techniques are required to compute the pressure

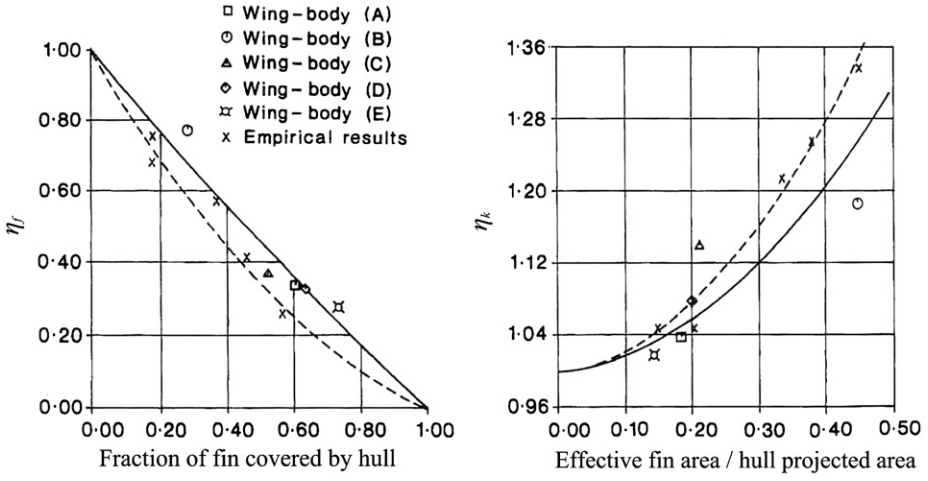

Fig. 5. Efficiency factors (solid line: experimental [27]; dashed line: CFD [55]).

distribution when considering viscosity, since no analytical solution of the Navier–Stokes equations is available for airships.

The following suggestions can be made for future research on the development of effective aerodynamic models for airships. First, efforts should be made to develop and validate aerodynamic prediction methods for airships at high angles of attack, which are particularly relevant for low-speed and hovering flight. Second, given the lack of a large data base of test results on airships, CFD packages can be used to produce the required data to extend existing or to develop new aerodynamic computational formulations, as indicated by [55].

3. Flight dynamics

3.1. Flight tests

We begin this section with a brief review of airship flight test results. Reports on full-scale flight tests of airships are scarce in literature. During the golden age of airships, flight tests were performed to determine the drag force and turn radius of rigid airships, such as the British R-29 [56] and the American USS Los Angeles airships [57]. However, these experiments were conducted decades ago and the accuracy of experimental results was limited by the instrumentation and measurement techniques of that time. More advanced instrumentation has been used in the flight tests of modern airships, giving more accurate measurement results. For example, flight tests were performed on Skyship-500 airship in the Patrol Airship Concept Evaluation (PACE) program [58,59] in the 1980s and on the Lotte airship more recently [60]. In these tests, the responses to inputs of elevator, rudder, and throttle were measured.

We can summarize the flight test results by grouping them into three categories.

- Deceleration tests conducted in 1920s and 1930s were used to obtain the drag of old airships by measuring the velocity response during periods of zero thrust. The drag force was then deduced by using a 1-DOF model of an airship in straight, level, and neutral buoyancy flight [45]. However, a number of problems plagued this approach [19]. First, it was difficult to maintain a constant altitude in the deceleration flight and, consequently, elevator inputs and pitch rotation contaminated the data. Second, measurement time lags were not taken into account in the data processing. As a result, "airship zero-lift drag prediction based on a proper combination of scale model tests and the theoretical/empirical correction was (as of 1935) more accurate than full-scale measurements by means of deceleration tests." [19].
- Evaluation of airships' lateral maneuverability consisted of turn trials to determine their steady turn rate (yaw rate), radius R_T, and sideslip angle β for different rudder inputs. The test data showed that the yaw rate is a nonlinear function of the rudder input (see Fig. 6(a) for the turn rate results of the Skyship-500 [58], for example), and that the product of turn radius and sideslip, $R_T\beta$, is approximately constant for different rudder angles. Non-dimensionalized values of $R_T\beta$ obtained from experiments on some old British airships [23] are plotted in Fig. 6(b), where λ is an equivalent distance from the CV to the point of application of the total side force. More comments on steady turn flight will follow in Section 3.4.1.
- The flight test data was also used to identify the aerodynamic derivatives in linearized dynamics models of airships. This will be further discussed in Section 3.3.

In the following subsections, we first discuss methods to develop nonlinear and linear flight dynamics models of airships.

3.2. 6-DOF nonlinear models

A number of nonlinear flight dynamics models and simulation programs have been presented for airships. In these models, the airship is modeled as a rigid body with three translational and three rotational DOFs and hence, the dynamics model is composed of six nonlinear differential equations describing the translational and rotational dynamics. The dynamics equations of motion for an airship written in scalar form can be found in [25]. In matrix/vector form, they can be summarized as

$$\begin{bmatrix} m\mathbf{I}_{3\times3} & -m\mathbf{r}_G^{\times} \\ m\mathbf{r}_G^{\times} & \mathbf{J} \end{bmatrix} \begin{bmatrix} \dot{\mathbf{v}} \\ \dot{\boldsymbol{\omega}} \end{bmatrix} + \begin{bmatrix} m\boldsymbol{\omega}^{\times}\mathbf{v} - m\boldsymbol{\omega}^{\times}\mathbf{r}_G^{\times}\boldsymbol{\omega} \\ m\mathbf{r}_G^{\times}\boldsymbol{\omega}^{\times}\mathbf{v} + \boldsymbol{\omega}^{\times}\mathbf{J}\boldsymbol{\omega} \end{bmatrix} = \begin{bmatrix} m\mathbf{g} \\ m\mathbf{r}_G^{\times}\mathbf{g} \end{bmatrix} - \begin{bmatrix} \rho V_B\mathbf{g} \\ \rho V_B\mathbf{r}_V^{\times}\mathbf{g} \end{bmatrix} + \begin{bmatrix} \mathbf{F}_{AD} \\ \mathbf{M}_{AD} \end{bmatrix} + \begin{bmatrix} \mathbf{F}_C \\ \mathbf{M}_C \end{bmatrix} \tag{10}$$

where m is the total mass, including the hull, gas, gondola, fins, ballonets, etc., $\mathbf{J}$ is the inertia tensor; $\mathbf{r}_G$ and $\mathbf{r}_V$ are the position vectors of the center of gravity (CG) and the CV expressed in the body frame, respectively; and $\mathbf{g}$ is the acceleration of gravity. Vectors $\mathbf{F}_{AD}$, $\mathbf{M}_{AD}$ and $\mathbf{F}_C$, $\mathbf{M}_C$ denote the aerodynamic and control force and moment, respectively. Recall that $\mathbf{v}$ and $\boldsymbol{\omega}$ denote the linear and angular velocity vectors of the airship-fixed frame.

The left hand side of Eq. (10) represents the inertial forces on the airship, with the first term related to the acceleration and the second term representing the nonlinear centrifugal and Coriolis

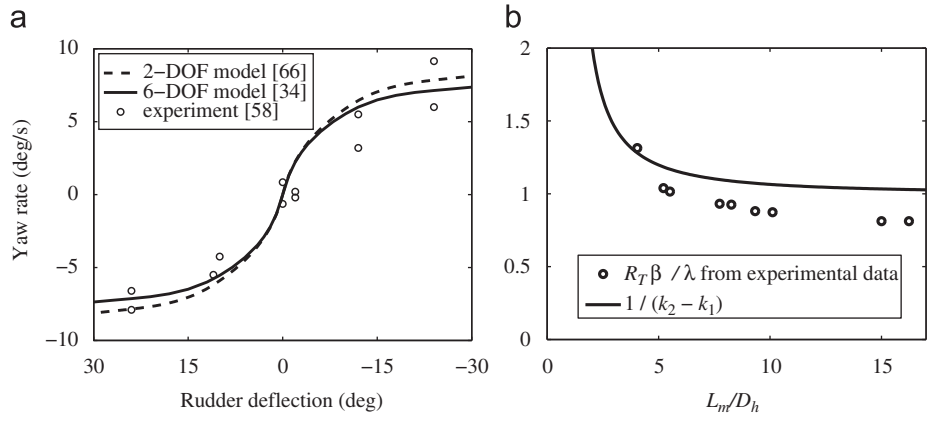

Fig. 6. Steady turn results: (a) turn rates of Skyship-500 at 12.86 m/s and (b) $R_T\beta/\lambda$ of some old British airships [23].

terms. The inertial parameters of the airship are required in Eq. (10). For a neutrally buoyant condition, the mass must be $m = \rho V_B$; however, determination of the CG's position vector $\mathbf{r}_G$ and the inertia tensor $\mathbf{J}$ require details on the design of the airship. It will be demonstrated in Section 3.4.1 that a simplified model can be used to predict steady turn rate, without the use of $\mathbf{r}_G$ and $\mathbf{J}$.

The right hand side of Eq. (10) includes the external forces and moments due to gravitational, aerostatic, aerodynamic, and control forces, respectively. In some models, the added-mass effects, incorporated here through $\mathbf{F}_{AD}$ and $\mathbf{M}_{AD}$, are treated as virtual inertia and are incorporated on the left hand side of Eq. (10); either approach must produce the same numerical results [61]. The control forces are due to thrusters and deflection the control surfaces. Prediction of control surface forces has been investigated thoroughly in the context of conventional aircraft, as for example, in [28], and these results will not be repeated here. The dynamics of thrusters is seldom discussed in the literature on airships.

Eq. (10) is written in the body-fixed frame at an arbitrary location, and the usual choice for the body frame's origin is different for airships and airplanes. Usually, for airplanes, the body-fixed frame is located at the CG (i.e., $\mathbf{r}_G = \mathbf{0}$) so that the centrifugal terms are eliminated and the translational and rotational accelerations are decoupled in the equations of motion. However, for airships, it is more convenient to establish the body-fixed frame at the CV ($\mathbf{r}_V = \mathbf{0}$) for two reasons: (1) the location of the CG can vary substantially during flight whereas the CV remain fixed, and (2) the computation of the added-mass matrix is simplified.

Flight dynamics models have been developed for several airships. One of the differences between these models is their approach to compute the aerodynamics. Amann [62] adopted the aerodynamics model of Jones and DeLaurier [27] in a nonlinear dynamics simulation program to predict the time responses due to different control inputs for the Skyship-500 airship (see Fig. 7(a)). Li and Nahon [34] unified a series of aerodynamic computational methods for the nonlinear dynamics simulation of the same airship. Wind-tunnel data can also be used to determine the aerodynamic characteristics needed in nonlinear flight dynamics simulation. For example, Gomes [25] imported the wind-tunnel aerodynamic coefficient results into their ACSL nonlinear simulation program for the YEZ-2A airship (see Fig. 7(b)) and used interpolation and extrapolation of the discrete data points to calculate the aerodynamic forces and moments.

Flight dynamics of *unconventional* airships have also been studied. NASA jointly with Systems Technology, Inc. performed a feasibility study of a hybrid heavy-lift airship, which consisted of a helium-filled envelope mounted on a frame with a helicopter at each corner, as displayed in Fig. 7(c). Ringland et al. [63] derived the nonlinear 6-DOF equations of motion and developed the simulation program HLASIM to evaluate this airship's flight characteristics, with a particular focus on the influence of high incidence and atmospheric turbulence on the flight response. It is noted that this type of hybrid airship has very different flight characteristics from conventional airships due to the aerodynamic lift forces generated by the helicopters.

3.3. Linear models and stability analysis

3.3.1. Linear models

The equations of motion (10) can be linearized with the assumption that the motion of the aircraft is constrained to small perturbations about a trimmed equilibrium flight condition. Linear dynamics models have been widely applied to study the flight behavior of airships, as for example in [64], and for control design, as is done in [12] for a large high-altitude airship. The linearized equations of motion can be divided into the longitudinal and lateral-direction sets, either of which can be written as

$$\mathbf{m}\dot{\mathbf{x}} = \mathbf{a}\mathbf{x} + \mathbf{b}\mathbf{u} \quad \text{or} \quad \dot{\mathbf{x}} = \mathbf{A}\mathbf{x} + \mathbf{B}\mathbf{u} \tag{11}$$

where $\mathbf{x}$ and $\mathbf{u}$ are the deviations of state and control vectors from the equilibrium condition, and $\mathbf{A} = \mathbf{m}^{-1}\mathbf{a}$, $\mathbf{B} = \mathbf{m}^{-1}\mathbf{b}$ are state and control matrices. The state and control vectors can be defined as $\mathbf{x} = [u,w,q,\theta]^{\mathrm{T}}$ and $\mathbf{u} = [T,\delta_e]^{\mathrm{T}}$ for the longitudinal motion, and $\mathbf{x} = [v,p,r,\phi]^{\mathrm{T}}$ and $\mathbf{u} = \delta_r$ for the lateral motion, where θ and ϕ are pitch and roll angles of the body-fixed frame, δ_e and δ_r are the elevator and rudder deflections, and T is the thrust force. Matrix $\mathbf{m}$ is the mass matrix, and $\mathbf{a}$ and $\mathbf{b}$ contain the derivatives of the external force or moment with respect to the corresponding states (refer to [3] for detailed expressions).

In formulating linear models of the Lotte airship (see Fig. 7(d)), Kornienko [60] found that some derivatives in $\mathbf{a}$ and $\mathbf{b}$ were insignificant and could be ignored, as listed in Table 2. For example, since the thruster of the Lotte airship is mounted at the rear of the

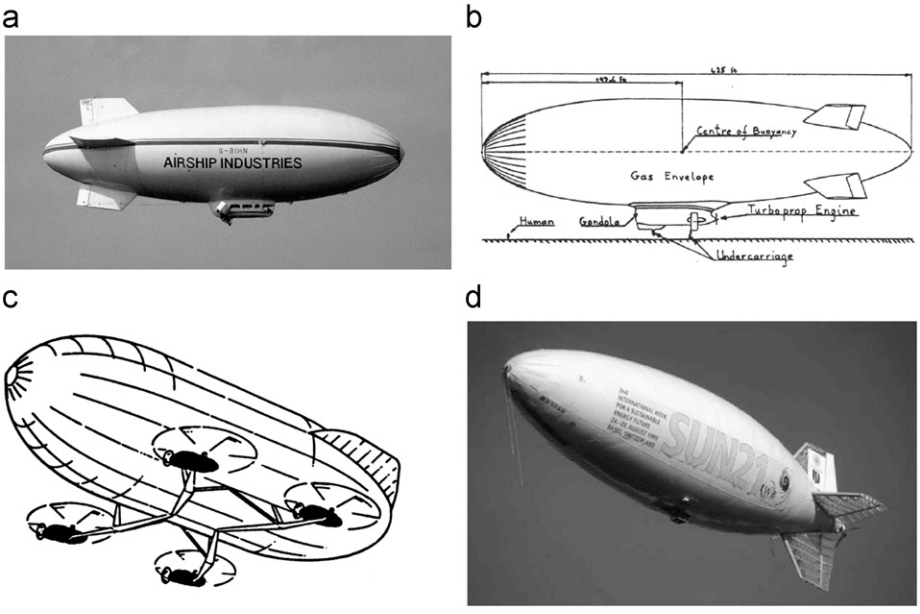

Fig. 7. Some simulated airships: (a) Skyship-500, (b) YEZ-2A [25], (c) hybrid heavy lift airship [63] and (d) Lotte [26].

hull, a thrust force perturbation only has a small influence on the pitch moment, yielding $\partial M_y/\partial T \approx 0$. However, this is not true if the thruster is mounted on the gondola, well below the CV, and therefore this derivative can be important for other airships.

Linear models can be calibrated by using wind-tunnel or flight test data. Jex and Gelhausen [59] adopted the HLASIM simulation program to calculate the aerodynamic derivatives in the linear dynamics model of the Skyship-500, and the matrices **A** and **B** were improved by using a frequency-domain fitting technique on the flight test data. Yamasaki and Goto [65] carried out a series of flight tests for the identification of matrices **m**, **a**, and **b** in the linear models for a small indoor airship, and the test data were analyzed with an extended least-squares algorithm to obtain the added mass and aerodynamic stability derivatives. Another model identification study of airship dynamics was conducted by Kornienko [60]. The responses of the Lotte airship due to inputs of throttle, elevators, rudders, and ailerons were measured and the flight test data was used to determine the aerodynamic derivatives with output-error and filter-error methods.

3.3.2. Stability analysis

Flight stability analysis is important for aircraft performance evaluation. Although most of the airship lift is generated by the aerostatic forces, the aerodynamic characteristics determine the stability of the aircraft. On the one hand, the streamlined hull experiences the aforementioned unstable pitch and yaw Munk moments; on the other hand, the viscous effects acting at the rear of the hull and the aerodynamic forces acting on the fins tend to stabilize the system. In addition, since the CG of an airship is located below the CV, the aircraft experiences oscillatory pitch and roll motion, similar to a pendulum. Stability has been analyzed for airships using analytical linear models [25,60,64] or numerical models obtained from finite differencing of the nonlinear equations [66]. These stability studies are carried out by evaluating the eigenvalues and eigenvectors of the state matrices of linear models.

Table 2
Insignificant derivatives in the linear models of the Lotte [60].

Forces and moments	Insignificant derivatives
Axial force F_x	$\partial F_x/\partial w$, $\partial F_x/\partial q$, $\partial F_x/\partial \delta_e$
Vertical force F_z	$\partial F_z/\partial u$, $\partial F_z/\partial \theta$, $\partial F_z/\partial T$
Pitch moment M_y	$\partial M_y/\partial u$, $\partial M_y/\partial T$
Side force F_y	$\partial F_y/\partial p$
Roll moment M_x	$\partial M_x/\partial v$, $\partial M_x/\partial r$
Yaw moment M_z	$\partial M_z/\partial p$, $\partial M_x/\partial \phi$

Stability analysis results in [25,60,64,66] reveal that conventional airships have similar motion characteristics for each mode. In the longitudinal plane, the first mode is a surge subsidence mode caused by aerodynamic axial drag, and can be considered as a 1-DOF surge motion u. The second longitudinal mode is a heave-pitch subsidence mode caused by the normal aerodynamic drag. The dominant motion is the heave motion w near zero speed, coupling with some pitch angle θ and pitch rate q as the speed increases. The third longitudinal model is a pitch-incidence oscillatory mode caused by the fact that the CG of an airship is located below the CV. Near zero speed, the dominant motion is the pitch rate q and as the speed increases, w becomes apparent. In the lateral plane, the first mode is a sideslip-yaw subsidence mode. Near zero speed, the most apparent motion is sideslip v and yaw rate r and with increasing speed, the roll rotation ϕ becomes apparent because of the centrifugal force. The second lateral mode is a yaw-roll subsidence mode, which is coupled with the first mode. The yaw rate and sideslip are dominant at near-zero speed and they couple with the roll rate p as the speed increases. The third lateral mode is a roll oscillation due to the offset of the CG from the CV. The readers are referred to [25,60,66] for detailed eigen diagrams for conventional airships at different speeds.

Only two modes can become unstable according to the stability analysis results in [25,60,64,66]. As the speed increases, the pitch-incidence oscillation mode and the sideslip-yaw subsidence mode of the Lotte airship become unstable, as illustrated by the eigenvalues at equilibrium forward speeds u_0 of 3, 4, 8, and 12 m/s in Fig. 8. This is because the unstable Munk moment dominates over the stabilizing moment generated by the fins [60]. All other modes become more stable as the speed increases, due to the increasing aerodynamic damping.

3.4. Simplified nonlinear models

3.4.1. For evaluation of steady turn characteristics

Steady turn characteristics are a key aspect in the evaluation of the lateral maneuverability of airships. A turn can be initiated by

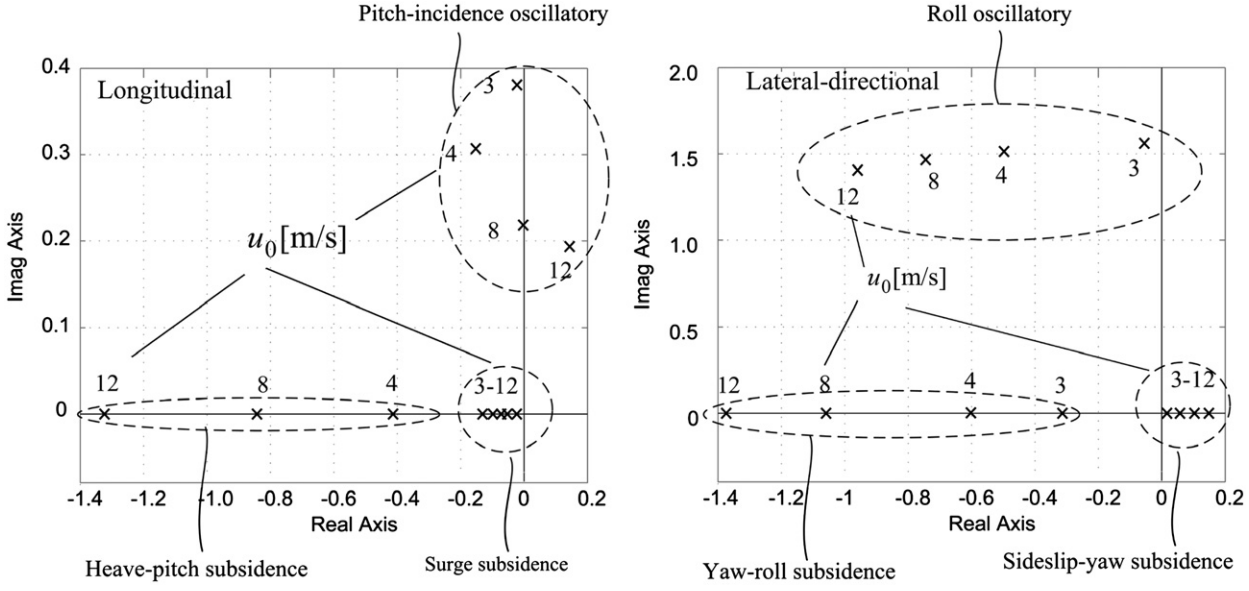

Fig. 8. Eigenvalues of the linear model of Lotte airship [60].

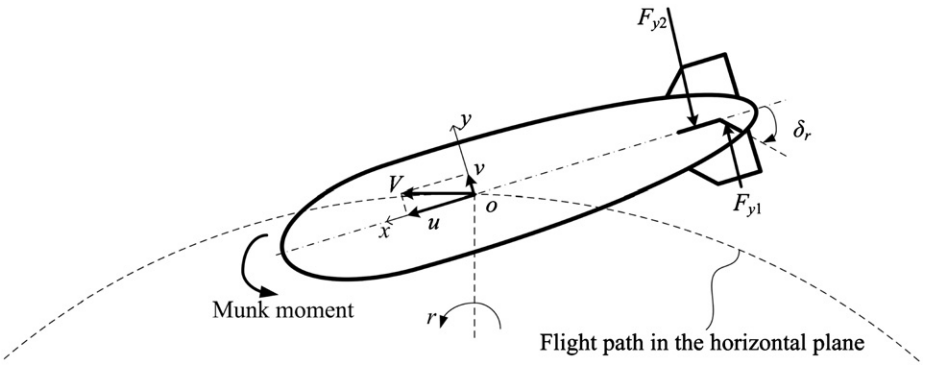

Fig. 9. An airship in a steady turn.

applying a rudder deflection input, as shown in Fig. 9. The airship with a forward speed u is given a rudder deflection δ_r with the trailing edge left, which generates a negative yaw moment and a positive lateral velocity v. This lateral velocity leads to a negative Munk yaw moment and the airship starts to turn with a negative yaw rate. This yaw rate and lateral velocity increase the aerodynamic force on the vertical fins resulting in a positive yaw moment. Once the moment from the rudder, the Munk moment, and the positive aerodynamic moment due to the fins cancel each other, the airship is in a steady turn.

Simplified models have been applied to predict the steady turn characteristics, and these require much less information than a full 6-DOF flight simulation. Jones [23] derived a simplified 2-DOF model to investigate the steady turn characteristics for the R-101 airship, with the aerodynamic derivatives measured from wind-tunnel experiments. Li [66] used a similar 2-DOF dynamics model to predict the steady turn rates for the Skyship-500. The result from the 2-DOF model was in agreement with the results from the full 6-DOF model and the flight tests (see Fig. 6(a)). The implementation of these simplified 2-DOF models requires only the dimensional information about the airship and does not require the position of CG and the inertia tensor. In addition, Jones [23] determined that the product of the turn rate and the sideslip $R_T\beta$ is approximately constant for different rudder deflections from the side force and yaw moment balance of an airship in a steady turn, i.e.,

$$\frac{R_T\beta}{\lambda} = \frac{1}{k_2 - k_1} \tag{12}$$

Recall that λ is an equivalent distance from the CV to the point at which the total side force acts. The curve of $1/(k_2-k_1)$ is plotted in Fig. 6(b) as a function of fineness ratio L_a/D_m. It should be noted that the aforementioned 2-DOF models and Eq. (12) can be used only for airships without auxiliary lateral thrusters, because the side force and yaw moment balance equations will change if auxiliary lateral thrusters are used.

3.4.2. For trajectory optimization

Simplified nonlinear models have been used for trajectory planning of stratospheric airships in the last few years. Bestaoui and Hima [67] carried out a preliminary study on the trajectory planning of a small blimp, using the 6-DOF nonlinear dynamics in the body-fixed frame with the assumption of trimmed flight, i.e., $\dot{\mathbf{v}} = \dot{\boldsymbol{\omega}} = \mathbf{0}$ in Eq. (10). Little information is given in [67] on the computation of aerodynamic coefficients. To overcome the limitation of trimmed flight, Lee and Bang [13] published a paper on the ascent trajectory optimization of a stratospheric airship in the presence of atmospheric turbulence. The airship is modeled as a point mass such that its rotational dynamics is ignored. The thrust, drag, buoyancy, and gravitation forces are incorporated into the calculation of the airspeed, flight path angle, and heading angle, with the lift and drag forces obtained from wind-tunnel tests. This point-mass model is then used to obtain the ascent trajectories with minimum time or minimum energy. Mueller et al. [68] used a dynamics model similar to that in [13] also for the ascent trajectory optimization of stratospheric airships. They further refined the dynamics model to account for the earth's rotation and the deflation of ballonets.

The simplification of a point-mass model is adequate for the applications considered in [13,68] because the flight path angle, heading angle, and bank angle are slowly varying so that the rotational dynamics of airships can be ignored. Unlike in the previous papers reviewed here, these models are established in a *wind-axes* local frame $\{ox_wy_wz_w\}$, whose orientation is different from the body-fixed frame in Fig. 1. The origin of the wind-axes frame is also on the airship but its x_w axis is aligned with the airship's speed relative to the wind rather than along the centerline. The use of the wind-axes frame to define the airship dynamics is consistent with normal practice in trajectory planning for airplanes [69]. However, care should be taken in the use of the wind-axes frame for airships because of potential difficulties in accounting for the added-mass effects. As pointed out in [70], the added-mass matrix $\mathbf{M}_{11}$ in Eq. (2), which is expressed in the body-fixed frame *oxyz* in Fig. 1, should be converted to the wind-axes frame using [70]

$$\mathbf{M}_{11,w} = \mathbf{C}_{wb}^{\mathrm{T}}\mathbf{M}_{11}\mathbf{C}_{wb} \tag{13}$$

where $\mathbf{C}_{wb}$ is the rotation matrix from the wind-axes frame to the body frame $\{oxyz\}$.

3.5. Summary

The main issues in the flight dynamics modeling of airships are the prediction of aerodynamic force and moment, as discussed in detail in Section 2, and the inertial parameters of the airship. Once these are properly formulated, the flight dynamics can be simulated using the nonlinear motion equations (10) or linear equations (11).

The flight characteristics of airships are different from those of airplanes due to the light lifting gas and the fact that the CG is well below the CV. The stability of an airship depends on whether the fin force and the restoring gravitational moment are sufficient to stabilize the vehicle against the unstable Munk moment. The modes of airships change dramatically with speed, implying that different controllers would be required for different speed regimes. Steady turn behavior is also primarily affected by the aerodynamic characteristics. For this reason, it is possible to predict the steady turn radius without using the inertial parameters. In addition to stability and lateral maneuverability analyses, flight dynamics modeling is also integral to the solution of trajectory optimization problems.

4. Incorporation of structural flexibility

4.1. Research issues

Unlike an airplane, for which the most significantly deformable components are the wings, the most flexible component of an airship is its hull. Based on the hull structure, airships fall into three main categories, namely, *rigid airships*, *non-rigid airships*, and *semi-rigid airships*. Rigid airships have a rigid hull frame containing multiple, non-pressurized gas cells or balloons to provide lift. Both semi-rigid and non-rigid airships use an inflated envelope as a hull and the hull shape is retained by a pressure level in excess of the surrounding air pressure. In contrast to non-rigid airships, semi-rigid airships have a rigid keel along the bottom of the envelope to distribute suspension loads onto the envelope. Non-rigid airships are the most common construction nowadays. Sufficient pressure difference between the surrounding air and the internal lifting gas is maintained across altitudes by inflating or deflating ballonets, which are air bags contained inside the hull (see Fig. 1). Unconventional hull structure designs, such as the double-hull airships and winged airships, have also been proposed in the past two decades and the readers are referred to [16] for more information on these designs.

Structural strength was a significant issue in the development of old rigid airships. For example, Evans [71] computed the force distribution due to aerostatic, aerodynamic, and inertial forces for the Shenandoah rigid airship and demonstrated the possibility of catastrophic failure due to the structural bending moment. To avoid the structural vulnerability, rigid designs are seldom used in modern airship construction and hence, we focus our attention on non-rigid and semi-rigid airships.

Research on modern airship structures is conducted from two perspectives: (1) material behavior and (2) fluid–structure interaction. Examples in the first category include the development of new airship envelope materials [72,73], experimental studies on the tear propagation of airship material [74], and the FEA stress analysis for the envelopes of LTA aircraft [75]. This review focuses on problems in the second category, since our interest is in airship dynamics. Research in fluid–structure interaction of airships addresses two issues: how an airship deforms in flight and how the deformation influences the aerodynamics and flight dynamics.

Although aeroelastic theories are well developed for airplanes [76] and techniques are available for modeling the mutual interaction between flexibility, aerodynamics, and flight dynamics of maneuvering HTA aircraft [77], only a few investigations have been reported on the fluid–structure interaction of LTA aircraft. There are two reasons for this. First, the LTA fluid–structure interaction problem is complex, especially in light of our far from mature understanding of their aerodynamics and structural behavior. Second, LTA aircraft fly at low speeds and the structural vulnerability and safety have been greatly improved for modern airships made of membrane structures, which make the fluid–structure interaction a less important issue in airship development. However, there has been growing interest in this problem over the last few years, partly because of the recent advances in computational capabilities which make it possible to solve the fluid–structure interaction problems, but also because of proposed new airship designs and materials.

Fig. 10(a) shows the Sanswire Stratellite airship, designed by Sanswire-TAO [78] for missions in the lower stratosphere up to 18,288 m (60,000 ft) altitude. The Stratellite is a segmented airship consisting of a sequence of buoyancy cells. Flight tests with the airship demonstrated large deformations of the hull which results from the relative displacement between the buoyancy cells. Therefore, the aerodynamics and flight dynamics models based on a rigid-body assumption, such as those reviewed in Sections 2 and 3, are not likely to be applicable to this very flexible airship.

Recently, very thin films have been proposed for high-altitude airships, for example, the High Platform II shown in Fig. 10(b), the first stratospheric airship in the world [79]. These materials were originally developed as part of NASA's Ultra Long Duration Balloon project and the thickness of the films can be as small as 0.038–0.048 mm [72,73]. Although they are very light and provide sufficient strength, these films have lower elastic moduli and are much thinner than conventional airship envelope materials such as Nylon and Dacron. Accordingly, the aeroelastic effects on the flight behavior could be important for the airships made of these unconventional composite materials.

4.2. Experimental studies

Experimental studies of airship fluid–structure interaction are very limited. Although there are no quantitative results on the structural deformation of airships (from wind-tunnel or flight tests), some qualitative observations can be gathered from the literature. Aeroelastic effects were observed for the old German Siemens-Schuckert airship in 1910s [80]. It was found that the airship was deformed like a banana due to side forces on the vertical tail planes. This indicates that bending was the main deformation of this airship.

Two German engineers, Hass and Dietzius, performed experiments on a non-rigid airship model filled with water, to investigate the validity of beam theory assumptions to describe the deformation of the airship [81]. After bending loads were applied to the model, it was observed that the cross-sections remained planar after the deformation. The authors of [81] found that the Navier hypothesis and Hooke's law may be assumed valid for the bending of non-rigid airship envelopes. As a result, the longitudinal tension stress of the envelope could be calculated as [81]

$$\sigma_L = \frac{Mc}{I} \tag{14}$$

where M is the internal bending moment, c is the distance to the neutral axis, which is the centerline of the airship, and I is the

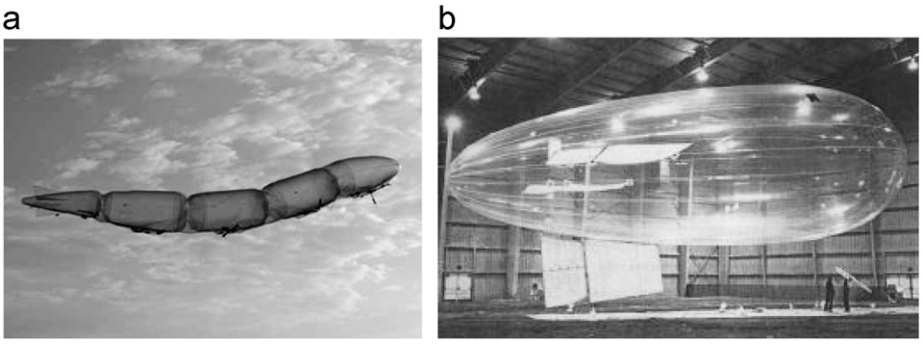

Fig. 10. (a) The Sanswire Stratellite airships [78] and (b) the High Platform II [79].

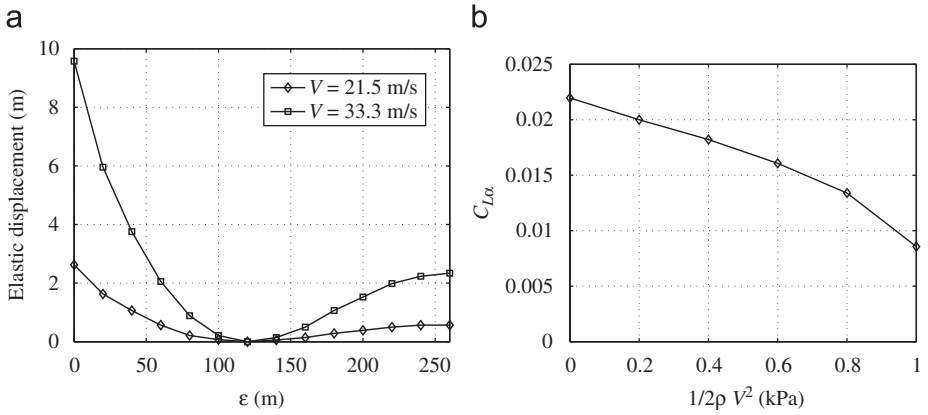

Fig. 11. Aeroelasticity simulation results from [82]: (a) deflection and (b) lift curve slope.

second moment of area about the neutral axis. This study indicates that the deflection behavior of a non-rigid airship can be represented using a bending beam model.

4.3. FEA and CFD methods

CFD packages have been used jointly with FEA modeling tools to study the aerodynamics of deformed airships. Amiryants et al. [82] investigated the aeroelasticity characteristics of a 260-m semi-rigid airship using FEA packages NASTRAN and ABAQUS for the structural analysis and using ARGON for the aerodynamics computation. They demonstrated that the first two modes of the airship could be described as beam-bending modes and, thus, a simplified beam model could be applied to compute the deflection of the airship. From their static aeroelastic analysis results, the airship deflected in a banana shape and considerable elastic displacement (maximum at the nose of approximately 3.7% of the total length) was observed in their simulation when the airship was at a sideslip of 5° with a speed of 33.3 m/s (see Fig. 11(a)). The lift on the forward part of the deformed airship increased, while that on the rear decreased as a result of hull bending. As shown in Fig. 11(b), the resulting lift curve slope $C_{L\alpha}$ decreases compared to the rigid model, for which $C_{L\alpha}$ remains constant at the zero-speed value, and this reduction becomes more obvious as the speed increases.

Bessert and Frederich [80] analyzed the effects of deformation on the lift coefficients C_L for the 260-m cargo lift CL-160 airship using the FEA package ABAQUS and CFD solver VSAERO. The fluid–structure interaction is accounted for by exchanging the geometric and aerodynamic solutions at every time step of the co-simulation. The resulting lift coefficients based on rigid-body, linear elastic, and nonlinear elastic models are compared in Fig. 12. The zero-lift angles of attack from the two elastic models are different from that of the rigid model due to the deformations. The lift curve slope $C_{L\alpha}$ from the linear elastic model is close to the rigid model. However, the nonlinear elastic model predicts a noticeably different slope. Unlike [82] where the lift curve slope $C_{L\alpha}$ is reduced by the deformation, the results in [80] show that the deformed airship has a larger $C_{L\alpha}$ than the rigid airship.

Other published results seem to indicate that the effects of structural flexibility are rather small. Omari [83] developed a numerical structure–fluid interaction solver based on a mixed element volume discretization. The deformation, vibration modes, and aerodynamic derivatives were calculated for an 1.37-m ellipsoidal membrane in an inviscid flow. The computed first and third modes of the body were beam-bending modes and the second mode was a membrane mode. The influence of elastic deformation on the lift coefficient was found to be small. Liu et al. [84] combined a nonlinear FEA model and a CFD model based on finite volume method for the

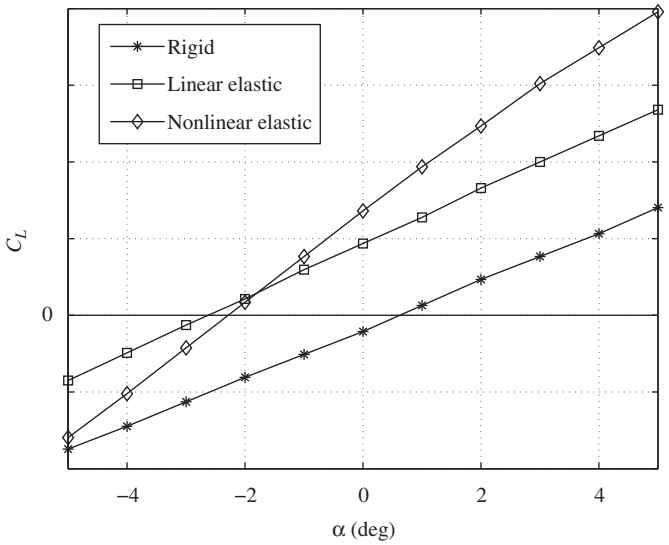

Fig. 12. Lift coefficient of an elastic airship [80] (values on the vertical axis were not provided in [80]).

aeroelastic analysis of several non-rigid airship hulls varying in length from 20 to 220 m. The lift coefficient results of these hulls are plotted in Fig. 13 and they show a relatively small effect of elasticity on C_L, albeit increasing slightly as the airship length increases.

It is difficult to draw any definitive conclusions based on the above works about the influence of deformation on airship aerodynamics, because there is little consistency in the findings reported in different papers. Also, the simulated airships have different physical and geometric parameters and the accuracy of the CFD and FEA packages may vary.

4.4. Analytical models

A few works have been published on analytical models for the fluid–structure interaction in airships, where researchers incorporate the structural deformation into airship flight dynamics. It should be noted that the effects of envelope wrinkling are not considered in these models. However, since wrinkling is a problem specific to in LTA aircraft and for the sake of completeness, the formulation of wrinkling criteria will also be reviewed here.

4.4.1. Dynamics models of maneuvering flexible airships

Venkatesan and Friedmann [85] conducted an aeroelastic analysis of the hybrid heavy lift airship, shown earlier in Fig. 7(c). The main

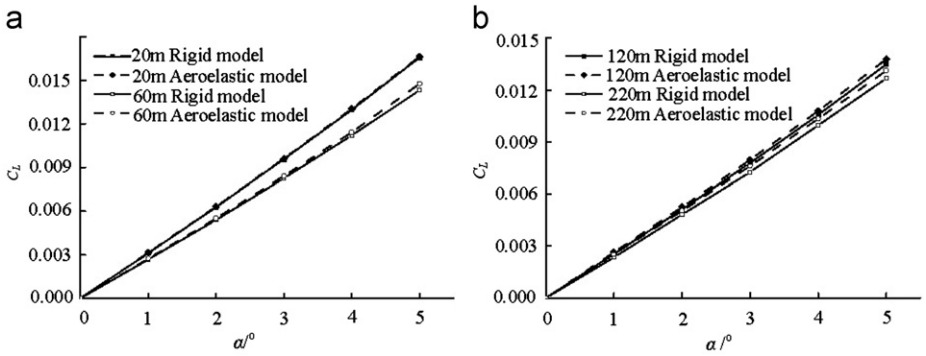

Fig. 13. Lift coefficients of elastic airship hulls in [84].

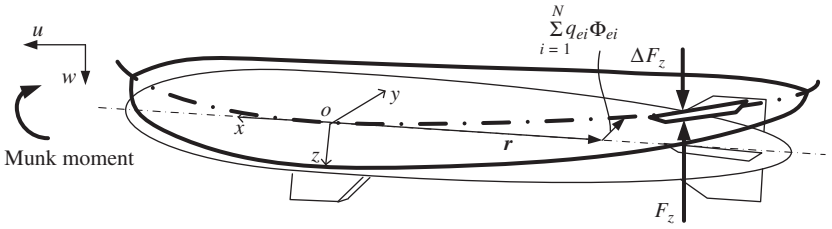

Fig. 14. An airship in bending.

concern in their work was the fluid–structure interaction between the helicopters and the supporting structure and thus it is not applicable to conventional airships. Bennaceur et al. [86] investigated the equations of motion of a flexible conventional airship with a particular focus on the effects of deformation on the inertial force. However, their formulation was limited by the potential fluid assumption and little discussion was given on the interaction between the flexibility and the aerodynamic forces.

Li et al. [87] proposed a theoretical framework for the dynamics modeling of flexible airships, which integrated the flight dynamics, structural dynamics, aerostatics, and aerodynamics. The elastic deformation was written as $\sum_{i=1}^{N} q_{ei}\mathbf{\Phi}_{ei}$, in which q_{ei} are the time-dependent generalized coordinates and $\mathbf{\Phi}_{ei}$ are the time-independent shape functions taken as natural vibration modes of an Euler–Bernoulli beam, and N is the number of shape functions. The normal force per unit length was predicted for the calculation of bending deflection. To capture the fluid–structure interaction, local velocity distribution on the deformed airship was used in the aerodynamics calculation, i.e.,

$$\mathbf{v}_d \approx \mathbf{v} + \boldsymbol{\omega}^{\times}\mathbf{r} + \sum_{i=1}^{N} \dot{q}_{ei}\mathbf{\Phi}_{ei} - u\sum_{i=1}^{N} q_{ei}\mathbf{\Phi}'_{ei} \tag{15}$$

where $\mathbf{r}$ is the position vector of a material point in the body-fixed frame, and the last two terms represent the local velocity due to deformation. The work of Li et al. [87] reveals two main results: first, the potential flow aerodynamics can significantly reduce the natural frequencies of an airship (by 25–30%), and second, the bending deflection reduces the stabilizing aerodynamic effects acting at the rear of the airship. With respect to the natural frequencies, similar conclusions have been reported for other vehicles moving in a heavy fluid, such as ships [88]. The second finding mentioned above can be explained by considering the schematic in Fig. 14, which shows a flexible airship moving with a forward speed u and a vertical downward speed w. The vertical speed leads to an upward aerodynamic force F_z at the rear due to viscosity and fins, which tends to stabilize the airship against the Munk pitch moment. Due to the bending deflection, the airship deforms in a nose- and tail-up banana shape. The upward deflection at the rear causes a decrease in the local angles of attack. This effectively produces a downward force ΔF_z, which reduces the stabilizing aerodynamic effects of viscosity and fin force. It is worth noting that the simulation results for the Skyship-500 in [87] demonstrate that this deformation-induced force ΔF_z is small for this airship due to its fairly high bending stiffness.

4.4.2. Wrinkling criteria

Wrinkling is a particular phenomenon that makes the structural characteristics of LTA aircraft different from those of HTA aircraft; by definition, it occurs when the stress of the inflated hull envelope becomes zero. The longitudinal and hoop membrane stresses for an inflated cylinder, in the absence of external loads, can be written as [89,90]

$$\sigma_L = \frac{pR}{2t}, \quad \sigma_H = \frac{pR}{t} \tag{16}$$

where t is the membrane thickness, R is the radius of the cylinder, and p is the internal pressure. As well, treating the cylinder as a beam, the longitudinal stress due to the bending moment M can be calculated from Eq. (14), with $c = R$. Wrinkling occurs when the maximum compressive stress due to bending equals to the longitudinal stress σ_L due to internal pressure, as in Eq. (16), yielding the wrinkling criterion for bending moment as [3]

$$M > \frac{p\pi R^3}{2} \tag{17}$$

A relationship between the wrinkling angle and the bending moment of the inflated cylinder can be further derived as [3]

$$\frac{M}{p\pi R^3} = \frac{\pi - \theta_w + \cos\theta_w \sin\theta_w}{2[\sin\theta_w + (\pi - \theta_w)\cos\theta_w]} \tag{18}$$

where the wrinkling angle θ_w defines the wrinkled portion in a cross section, as illustrated in Fig. 15. From that figure, one can see that the wrinkling starts at $M = p\pi R^3/2$ and as the bending moment increases to $p\pi R^3$, the wrinkling angle approaches π, i.e., the wrinkles propagate completely around the circumference of the cylinder.

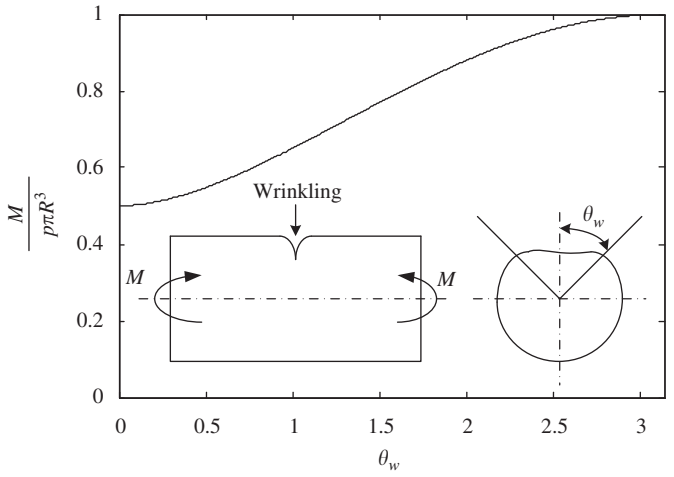

Fig. 15. Relationship of wrinkling angle and bending moment from Eq. (18).

A wrinkling criterion for the internal shear force is also derived in [89,90]. In shear, wrinkling occurs if the minimum principal membrane stress becomes zero. Under this condition, the maximum allowable shear stress can be determined for the hoop and longitudinal stresses in Eq. (16). The resulting wrinkling criterion is as follows:

$$Q > \frac{\pi p R^2}{\sqrt{2}} \tag{19}$$

where Q is the shear force.

The wrinkling criteria in Eqs. (18) and (19) are based on the stress analysis of an inflated cylinder. The cylindrical approximation of the airship hull can be justified by the fact that the highest bending moment and shear force occur in the central part of the hull [89,90]. Analysis accounting for the variation of cross-sectional radius can be found in [89,90], where it is also shown that the difference in stresses obtained with and without the constant-radius assumption are small ($<5\%$) near the middle of the hull.

To use Eqs. (18) and (19), the bending moment and shear force values must be first obtained. An empirical prediction method for the maximum bending moment on the airship hull is given in [3] which is useful for a preliminary check of internal pressure. A more accurate calculation of bending moment and shear force requires the external normal force distribution along the hull; it in turn can be computed with the methods discussed in Section 2.

4.5. Summary

Based on the existing research, there is no strong evidence that the flexibility effects have a significant impact on the flight characteristics of conventional modern airships. However, these effects could become important when the inflated hull structure wrinkles or when the natural frequencies of the flexible modes become sufficiently low so as to interact with the rigid-body modes, for example, if the airship were constructed of very thin materials. Furthermore, for unconventional airships with large deformation, such as the Sanswire Stratellite airship in Fig. 10(a), the aeroelastic effects must be taken into account in the dynamics modeling.

Current analytical models for the aeroelastic analysis of airships are limited and there are no effective tools to predict the aeroelastic effects on the flight characteristics. Application of FEA and CFD codes is hindered by their high computational cost. It is difficult to draw general conclusions based on the above FEA and CFD works. At this point, many outstanding questions remain, for example: What effect does structural deformation have on the lift coefficient and the lift-curve slope? How do these effects scale with airship size? Furthermore, predictions from different FEA and CFD packages need to be compared by employing a set of benchmark tests.

The following suggestions can be made for future research on fluid–structure interaction in airships. First, efforts should be made to derive simple analytical aeroelastic models for airships, for example, to predict the fin force reduction due to bending deflection as indicated in [87]. Second, prediction methods should be developed for the influence of wrinkling on the aerodynamics and flight dynamics. Third, efforts should be made to investigate the aeroelastic characteristics of unconventional airship designs made of very thin films or with large deformation.

5. Incorporation of atmospheric turbulence

As with LTA aircraft, an airship's flight characteristics can be strongly affected by atmospheric turbulence. In this section, we focus on how to incorporate a particular representation of atmospheric turbulence into the airship dynamics model. The issue of how to obtain the atmospheric turbulence (either by measurements or modeling) is beyond the scope of this review. Readers are referred to [91] for a detailed presentation on the modeling of atmospheric turbulence.

5.1. Experimental studies

Quantifying the motion response of an airship to the atmospheric turbulence through flight tests is a difficult task, since this requires simultaneous measurements of airship motion and turbulent wind. Little data on atmospheric turbulence and the corresponding dynamic response have been collected in the flight tests discussed in Section 3. Turbulent wind can be simulated in a wind tunnel and this technique has been used to measure the airship aerodynamics in turbulence. But even such data are limited in literature.

Lagrange [92] carried out an experimental study of the aerodynamic force on a 0.76-m (30-in) scaled airship model in vertical turbulence. Isotropic random turbulent flow was created in a wind tunnel by using flow through a grid. The turbulence angle of attack was defined as $\alpha_g = w_g/V$, in which w_g is the vertical gust velocity and V is the air speed. The following power spectral densities were measured: of the turbulence input $\Phi_{\alpha_g\alpha_g}$, of the normal force coefficient $\Phi_{C_NC_N}$, and of the pitch moment coefficient $\Phi_{C_MC_M}$. The resulting transfer functions $\Phi_{C_NC_N}/\Phi_{\alpha_g\alpha_g}$ and $\Phi_{C_MC_M}/\Phi_{\alpha_g\alpha_g}$ for bare hull and hull–fin combination are plotted in Fig. 16 against the wave number $\Omega = 2\pi f/V$, where f is the frequency in Hz. For the bare hull, there is no peak in the pitch moment response but a peak for the normal force occurs at $\Omega = 3.9\ \mathrm{m}^{-1}$ ($1.2\ \mathrm{ft}^{-1}$). This wave number corresponds to a turbulence wave length of about twice the hull length of the airship model. The addition of fins dramatically changes the aerodynamic response to turbulence. The peak present in the normal force response of the bare hull disappears while there is a peak in the moment response curve. One can also observe an increase in the steady value of C_N (at $\Omega = 0$) and a decrease in the steady value of C_M due to the fins.

5.2. Theoretical methods

Two approaches have been used to incorporate atmospheric turbulence into airship dynamics models. The first is an energy-based method, where the turbulent air flow is assumed to be inviscid and the force and moment due to the flow motion is derived from the kinetic energy of the fluid. This method focuses on the coupling between the flow motion and the added-mass

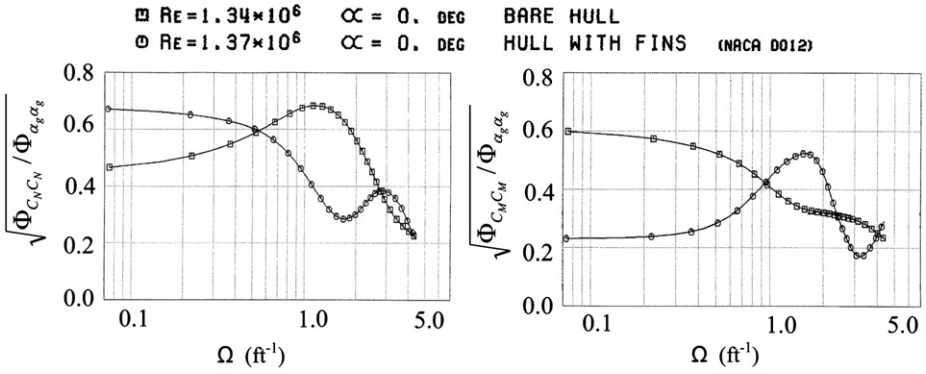

Fig. 16. Turbulence response of normal force and pitch moment in [92].

aerodynamic terms. Thus, it can be considered as an extension of the derivation of the added-mass force and moment in Section 2.2 where the added-mass terms are derived from kinetic energy via Kirchhoff's [30,17]. The second method is based on the slender body theory. In this method, the turbulence is first incorporated into the aerodynamic computation for each cross-section along the airship, and then the total force and moment are obtained by integrating the local force distribution over the airship. This method can be considered as an extension of Munk's equation (1) or Jones and DeLaurier's slice method in [27].

5.2.1. Energy method

The energy-based method was proposed to investigate the influence of flow turbulence on airship aerodynamics in the golden age of airships. Taylor [93] derived the forces on a small stationary body immersed in a non-uniform potential fluid from the fluid kinetic energy. A practical application of this work is the correction of the axial drag measurement on old airship models in wind-tunnel tests. It was found that the airship models tested in a wind tunnel experience a horizontal force due to the spatial gradients of flow velocity as follows:

$$F_{fx} = (1+k_1)m' u_f \frac{\partial u_f}{\partial x} \tag{20}$$

where u_f is the flow velocity at the CV in the absence of the body. Recall that m' is the mass of the displaced air and k_1 is the translational added-mass factor along the x axis. It can be seen from Eq. (20) that the added-mass terms are coupled with the spatial gradient of flow velocity.

The fluid dynamic force on a body in a non-uniform potential fluid has also been studied in the field of hydrodynamics. Newman [31] extended Eq. (20) to account for the acceleration of an unsteady fluid and the body velocity in the x direction u, yielding

$$F_{fx} = (1+k_1)m' \left[\dot{u}_f + (u_f - u)\frac{\partial u_f}{\partial x} \right] \tag{21}$$

Lewis et al. [94] presented the equations of motion for an underwater vehicle, incorporating the velocity and acceleration of the water flow. Some errors in [94] were found and corrected by Thomasson [35] in 2000 when he tried to apply the equations in [94] to airships.

Thomasson [35] derived a new set of motion equations for a 6-DOF rigid-body vehicle in an unsteady and non-uniform heavy fluid. In this work, the vehicle is assumed to be small so that the changes in the velocity of the undisturbed flow over the length of the vehicle are small relative to the flow velocity [35]. Under this assumption, the flow velocity distribution in the absence of the vehicle can be obtained from the first-order Taylor expansion about the velocity at the location of the body-frame origin, i.e.,

$$\mathbf{v}_{f,\mathbf{r}} = \mathbf{v}_f + \mathbf{\Phi}_v^{\mathrm{T}}\mathbf{r}, \quad \text{where } \mathbf{\Phi}_v = \begin{bmatrix} \frac{\partial u_f}{\partial x} & \frac{\partial v_f}{\partial x} & \frac{\partial w_f}{\partial x} \\ \frac{\partial u_f}{\partial y} & \frac{\partial v_f}{\partial y} & \frac{\partial w_f}{\partial y} \\ \frac{\partial u_f}{\partial z} & \frac{\partial v_f}{\partial z} & \frac{\partial w_f}{\partial z} \end{bmatrix} \tag{22}$$

where $\mathbf{v}_f = [u_f, v_f, w_f]^{\mathrm{T}}$ is the flow velocity at the location of the body-frame origin, $\mathbf{r}$ is the position vector of a point of interest from that location, and $\mathbf{\Phi}_v$ contains the spatial gradients of the non-uniform flow velocity at the origin. All vectors in Eq. (22) are expressed in the body frame. Thomasson derived the change of the kinetic energy of the fluid due to the presence of the vehicle and developed the motion equations using Lagrange's equations. The results of [35] are summarized now, but with some changes in form and notation for consistency of presentation. First, the body frame in [35] can be located at an arbitrary position on the vehicle, while in this paper, the body frame is established at the CV and hence, the terms related to the position of CV in [35] are dropped. Second, the fluid velocity in [35] is split into two terms, one representing a uniform current with no spatial gradients and the other one representing a circulating flow with spatial gradients. In this paper, the two terms are combined in $\mathbf{v}_f$ for a more compact representation. Third, the fluid dynamic terms due to flow motion in [35] are mixed with the inertial terms in the motion equations. Since the inertial terms have already been presented in Eq. (10), they are not repeated in the following.

With the above changes, the force due to the fluid motion extracted from [35] is given as follows:

$$\begin{aligned} \mathbf{F}_f = {} & \mathbf{M}_{11}\dot{\mathbf{v}}_f + \boldsymbol{\omega}^{\times}\mathbf{M}_{11}\mathbf{v}_f + m'\dot{\mathbf{v}}_f + m'\boldsymbol{\omega}^{\times}\mathbf{v}_f - \mathbf{\Phi}_v\mathbf{M}_{11}(\mathbf{v}-\mathbf{v}_f) \\ & - m'\mathbf{\Phi}_v(\mathbf{v}-\mathbf{v}_f) - \mathbf{\Phi}_v\mathbf{M}_{12}\boldsymbol{\omega} \end{aligned} \tag{23}$$

Recall that $\mathbf{M}_{11}$ and $\mathbf{M}_{12}$ are block matrices in the added-mass matrix in Eq. (2). It can be verified that the x component of the force in Eq. (23) reduces to the force in Eq. (21) for an axisymmetric vehicle in pure translation, and it can be further reduced to Eq. (20) if the vehicle is stationary and the fluid flow is steady. The total potential fluid force is the sum of $\mathbf{F}_f$ in Eq. (23) and $\mathbf{F}_A$ in Eq. (2), respectively, i.e.,

$$\begin{aligned} \mathbf{F}_A + \mathbf{F}_f = {} & -\mathbf{M}_{11}(\dot{\mathbf{v}}-\dot{\mathbf{v}}_f) - \mathbf{M}_{12}\dot{\boldsymbol{\omega}} - \boldsymbol{\omega}^{\times}\mathbf{M}_{11}(\mathbf{v}-\mathbf{v}_f) - \boldsymbol{\omega}^{\times}\mathbf{M}_{12}\boldsymbol{\omega} \\ & + m'\dot{\mathbf{v}}_f + m'\boldsymbol{\omega}^{\times}\mathbf{v}_f - \mathbf{\Phi}_v\mathbf{M}_{11}(\mathbf{v}-\mathbf{v}_f) - m'\mathbf{\Phi}_v(\mathbf{v}-\mathbf{v}_f) - \mathbf{\Phi}_v\mathbf{M}_{12}\boldsymbol{\omega} \end{aligned} \tag{24}$$

In other words, to incorporate the force due to the flow motion, one can replace $\dot{\mathbf{v}}$ with $\dot{\mathbf{v}}-\dot{\mathbf{v}}_f$ and $\mathbf{v}$ with $\mathbf{v}-\mathbf{v}_f$ when computing $\mathbf{F}_A$ and then add the terms related to m' and $\mathbf{\Phi}_v$ (the second line of Eq. (24)).

The total potential fluid moment is accordingly from [35]

$$\mathbf{M}_A+\mathbf{M}_f=-\mathbf{M}_{21}(\dot{\mathbf{v}}-\dot{\mathbf{v}}_f)-\mathbf{M}_{22}\dot{\boldsymbol{\omega}}-(\mathbf{v}^\times-\mathbf{v}_f^\times)\mathbf{M}_{11}(\mathbf{v}-\mathbf{v}_f)$$
$$-(\mathbf{v}^\times-\mathbf{v}_f^\times)\mathbf{M}_{12}\boldsymbol{\omega}-\boldsymbol{\omega}^\times\mathbf{M}_{21}(\mathbf{v}-\mathbf{v}_f)-\boldsymbol{\omega}^\times\mathbf{M}_{22}\boldsymbol{\omega} \quad (25)$$

Recall that $\mathbf{M}_{21}$ and $\mathbf{M}_{22}$ are also block matrices in the added-mass matrix (see Eq. (2)). We can observe from Eq. (25) that the velocity gradient matrix $\boldsymbol{\Phi}_v$ has no influence on the moment if the body frame is established at the CV. As well, to incorporate the moment due to the flow motion, one can simply replace $\dot{\mathbf{v}}$ with $\dot{\mathbf{v}}-\dot{\mathbf{v}}_f$ and $\mathbf{v}$ with $\mathbf{v}-\mathbf{v}_f$ in the calculation of $\mathbf{M}_A$.

Azinheira et al. [95] investigated the wind influence on airship dynamics via a Newtonian approach. Recently, they found that an inertial moment term is missing in [95] and they corrected the moment result via a Lagrangian approach [96]. In these two articles, Azinheira et al. incorporated the linear velocity and acceleration ($\mathbf{v}_f$ and $\dot{\mathbf{v}}_f$) and angular velocity and acceleration ($\boldsymbol{\omega}_f$ and $\dot{\boldsymbol{\omega}}_f$) of the wind into the equations of motion. The angular velocity $\boldsymbol{\omega}_f$ represents the flow vorticity and can be obtained from the gradient matrix $\boldsymbol{\Phi}_v$. The matrix $\boldsymbol{\Phi}_v$ is split into symmetric and antisymmetric parts, with the symmetric representing the irrotational strain rates and the antisymmetric representing the vorticity. Readers are referred to literature on atmospheric turbulence modeling, such as [91], for how to obtain $\boldsymbol{\omega}_f$ from $\boldsymbol{\Phi}_v$. The force result in [95] is in agreement with Thomasson's equation (23), except that the matrix $\mathbf{M}_{12}$ is assumed to be zero and the force related to the spatial gradients of wind velocity is not considered in [95]. However, additional terms due to $\boldsymbol{\omega}_f$ and $\dot{\boldsymbol{\omega}}_f$ appear in the moment result presented in [96]

$$\mathbf{M}_f(\boldsymbol{\omega}_f,\dot{\boldsymbol{\omega}}_f)=(\mathbf{J}'+\mathbf{M}_{22})\dot{\boldsymbol{\omega}}_f+\boldsymbol{\omega}^\times(\mathbf{J}'+\mathbf{M}_{22})\boldsymbol{\omega}_f \quad (26)$$

where $\mathbf{J}'$ is the inertia tensor of the displaced air. Therefore, besides the terms in Eq. (25), one can add the terms in Eq. (26) to account for the vorticity of the wind. Azinheira et al. analyzed the influence of constant wind in the longitudinal and lateral directions on the stability modes of an airship moving with low speeds [95]. Under longitudinal wind, the frequency of pitch oscillation mode decreases and the frequency of the roll oscillation mode increases as the longitudinal wind speed increases. Under lateral wind, the lateral modes are insensitive to the wind, but the pitch oscillation exhibits a lower damping ratio and a lower frequency as the wind speed increases. However, we caution readers to be careful in using these stability results since the inertial moment term in [95] is incorrect.

The following limitations of the energy-based method employed in [35,95,96] should be noted. First, the aerodynamics due to viscosity and the lift and drag on tail fins are not considered in these works. To account for the flow motion, relative velocity between the body and the air should be used in the calculation of these aerodynamic terms. Second, Eqs. (23)–(26) are derived based on a small-body assumption. The applicability of these equations to large airships is uncertain. Third, Eqs. (23)–(26) are "point" equations and do not provide the force distribution along an airship in turbulent wind, which is required for structural analysis.

5.2.2. Slender body method

Based on the slender body theory, the force on a cross-section of a slender body can be calculated from the cross flow in the plane of that cross-section. Then, the aerodynamic force on a cross-section of an airship moving in a turbulent wind can be obtained from the local turbulent flow in that cross-sectional plane. Compared to the inviscid flow assumption of the energy-based approach, the slender body theory allows for a more general modeling of the turbulent wind field.

As illustrated in Fig. 17, the turbulent wind can be represented as a superposition of a mean wind speed and a small space-dependent gust speed as

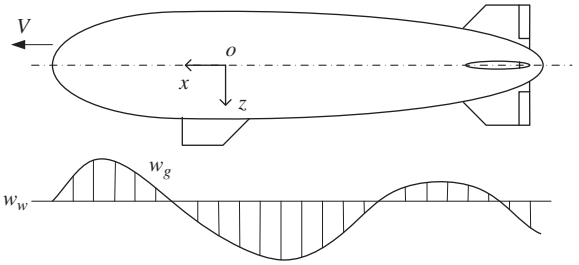

Fig. 17. Airship in vertical turbulence.

$$\mathbf{v}_{f,\mathbf{r}}=\mathbf{v}_w+\mathbf{v}_g(\mathbf{r}) \quad (27)$$

Compared to Eq. (22), the second term in Eq. (27) can be an arbitrary small disturbance. The mean wind speed $\mathbf{v}_w$ is taken into account by using the relative speed $\mathbf{v}-\mathbf{v}_w$ to calculate the angle of attack and dynamic pressure in the aerodynamic computation, for example, in Eqs. (1), (5), or (7). The gust $\mathbf{v}_g$ is incorporated as an additional term, as discussed below.

Calligeros et al. [97] and Lagrange [92] calculated the normal force for an airship traveling with a forward speed V through a vertical gust represented by w_g (see Fig. 17). The normal force on a local cross-section due to the vertical gust is [92]

$$\frac{dF_{Ng}}{d\varepsilon}=2q_0\alpha_g\frac{dS}{d\varepsilon} \quad (28)$$

where recall that $\alpha_g=w_g/V$. Eq. (28) is similar to Eq. (1), except that α is replaced by a small gust-induced angle of attack α_g and that the added-mass factors are not incorporated. Lagrange [92] compared the frequency responses of normal force and pitch moment calculated from Eq. (28) to wind-tunnel test results in Fig. 16, but considerable error was observed. This was likely because the airship was not slender (with fineness ratio of 4) and the added-mass factors were not included to account for the finite length in Eq. (28).

DeLaurier et al. [98] and Layton et al. [99] extended the aerodynamic computational approach in [27] to incorporate the gust into the aerodynamics model. The normal force distribution due to the gust is obtained as [98]

$$\frac{dF_{Ng}}{d\varepsilon}=(k_2-k_1)\eta_k q_0\frac{dS}{d\varepsilon}\left[\sin(2\alpha+2\alpha_g)\cos\left(\frac{\alpha}{2}+\frac{\alpha_g}{2}\right)-\sin(2\alpha)\cos\frac{\alpha}{2}\right] \quad (29)$$

Comparing to Eq. (7), we can see that the influence of small gust on the viscous term is ignored here. If $\alpha=0$, α_g is small, and the factor $(k_2-k_1)\eta_k$ is assumed to be unity, Eq. (29) reduces to Eq. (28). DeLaurier et al. [98] calculated the frequency responses of aerodynamic force, velocities, bending moment, and shear force to random gust for the Akron airship. It was found that the peak normal force and pitch moment due to gust occur at wave number $\Omega=0.033\ \mathrm{m}^{-1}$ ($0.01\ \mathrm{ft}^{-1}$) and $0.016\ \mathrm{m}^{-1}$ ($0.005\ \mathrm{ft}^{-1}$), respectively. These wave numbers correspond to wave lengths of the order of magnitude of the airship length (239 m). The motion response is dependent upon the control gains for the elevator deflection, implying that atmospheric turbulence should be considered in the controller design. In addition, the simulation results in [98] show that the gust has only a small influence on the bending moment and shear force.

Compared with the energy-based method, the slender body-based method has an advantage that the turbulence field can be described more accurately relative to Eq. (22). Furthermore, because the turbulence is incorporated through the normal force distribution, the slender body-based method can be used to obtain the shear force and bending moment distributions resulting from atmospheric turbulence.

On the other hand, the modeling employed in [97–99] implies a frozen-field turbulence, i.e., the turbulent velocities do not change during the time of passage of the aircraft. This is true for most flight conditions of airplanes [91] but has been argued inappropriate for LTA aircraft due to their much lower flight speeds [63]. As such, the flow acceleration ($\dot{\mathbf{v}}_w$ and $\dot{\mathbf{v}}_g$) may need to be considered in airship dynamics.

5.3. Summary

The articles [35,95,96] have advanced our understanding of the coupling between the flow motion and the added-mass aerodynamic terms. The energy-based method employed in these papers characterizes an inviscid fluid by the flow velocity, acceleration, and spatial velocity gradients at a single point (the CV of an airship which is small compared to the turbulence wave length). In the slender body-based method used in [97–99], the flow field is decomposed into mean wind velocity and a space-dependent gust velocity, and then the force on each cross-section of the airship is computed from the gust angle of attack at that position. This method can be used for large airships but the flow acceleration should be incorporated. A possible scenario to extend the energy-based approach to large airships would be to discretize the airship into a series of small slices and introduce a multi-point turbulence model to describe the turbulence velocity and acceleration at the center of each slice. The force and moment on each slice due to the turbulence can be obtained using the energy-based method. Then, the total force and moment could be computed by summation of those on the slices.

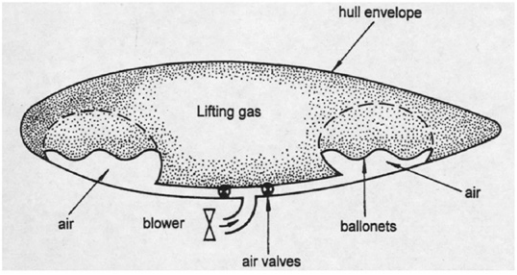

Fig. 18. Pressure control system in a non-rigid airship [3].

6. Incorporation of effects of ballonets

Ballonets are components particular to LTA aircraft, used to control buoyancy and to maintain sufficient pressure difference between the surrounding air and the internal lifting gas across the hull envelope. Typically two or three in number, they are air bags contained inside the hull, inflated or deflated by means of a blow fan as drawn in Fig. 18. Pressure height is the airship height at which all the ballonets are empty and the internal pressure can no longer be controlled by the deflation or inflation of ballonets [3]. To reach a pressure height of 4 km, the ballonet can occupy up to 50% of the hull volume at low altitude [100]; for a stratospheric airship designed to fly at an altitude of approximately 20 km, the ballonet volume can be 90% of the hull volume at sea level [101]. These numbers imply that the ballonets could strongly affect the dynamics characteristics of an airship, particularly if they move or deform as a result of airship motion. The influence of ballonets on airship dynamics depends on their size and shape and how they are attached to the hull envelope. In addition, the airship becomes a variable mass system due to the inflation and deflation of ballonets. To date, a very limited number of experimental and theoretical studies on ballonets can be found in literature.

6.1. Experimental studies

Nakadate [102] conducted ballonet tilting tests for the SPF-2 airship with a water model and an air/helium model, with the ballonet filled in stages up to 100% fullness. It was found that the shape of the ballonet is preserved without significant deformation at different pitch angles, and matches reasonably well with FEA results from MSC.Dytran. The variation of ballonet volume and the hull internal pressure at different altitudes have also been measured in a flight test of the SPF-2 [102], as displayed in Fig. 19(a).

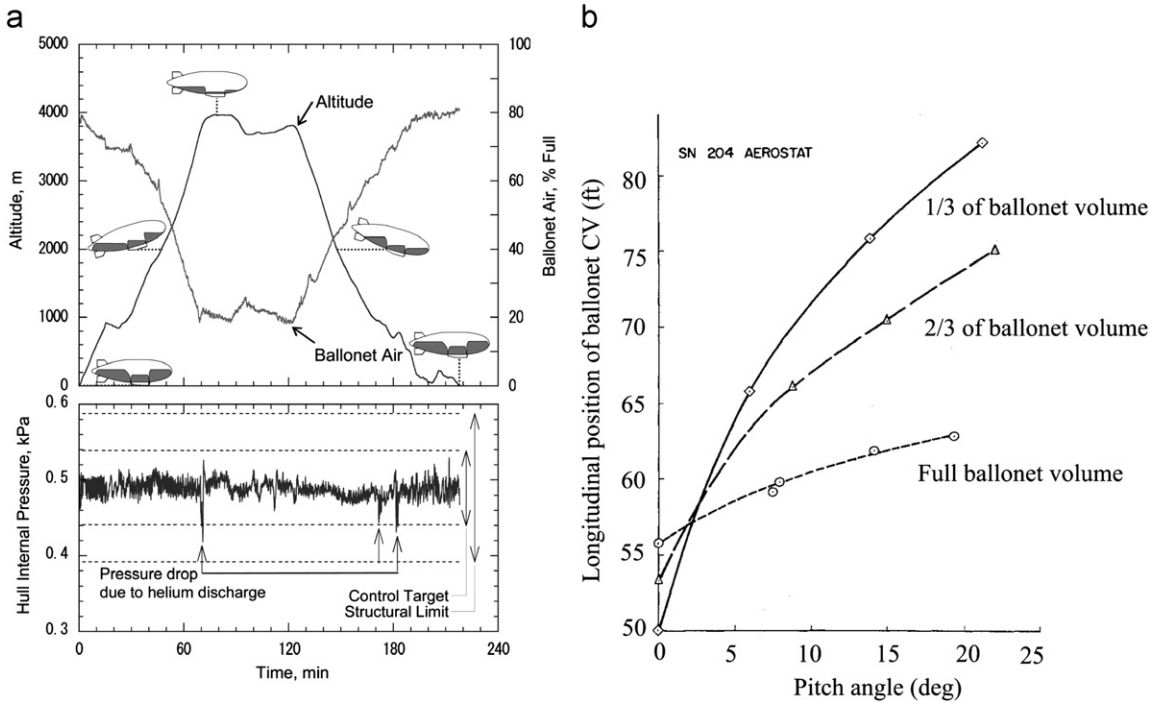

Fig. 19. (a) Altitude, ballonet volume, and hull pressure for the SPF-2 airship [102] and (b) ballonet CV position for the SN-200 aerostat [103].

The ballonets are filled to approximately 80% of their full size at an altitude of 1000 m and reduced to 20% at 4000 m, so that the differential pressure between the lifting gas and the surrounding air is maintained within the structural limits. Another observation is that the ballonets did not experience a sloshing problem during the flight tests [102,100].

DeLaurier [103] reported the experimental data of the ballonet CV position for the 50-m (163-ft) SN-204 aerostat, at different pitch angles (see Fig. 19(b)). Tests were carried out for three cases with air occupying 1/3, 2/3, and the whole of the ballonet envelope. It can be seen from Fig. 19(b) that the ballonet CV location is affected by the aerostat pitch angle. In particular, with the ballonet 1/3 full, the variation of the ballonet CV location is as high as 20% of the aerostat length. This indicates the coupling between ballonet motion and pitch rotation. These data were used for the parameter identification of a semi-empirical model for ballonet sloshing [103], which will be further discussed in Section 6.3.

6.2. Theoretical models

Cai et al. [104] formulated the equations of motion for an airship with the ballonets modeled as points at fixed positions and variable masses. The variation of the mass matrix (see Eq. (10)) due to the ballonet inflation and deflation is taken into account in their equations. That is, the total mass, position vector of CG, and the second moment of inertia are written as [104]

$$m=\overline{m}+\sum_{k=1}^{N_b}\Delta m_{bk},\quad \mathbf{r}_G=\overline{\mathbf{r}}_G+\frac{1}{m}\sum_{k=1}^{N_b}\Delta m_{bk}\mathbf{r}_{bk},\quad \mathbf{J}=\overline{\mathbf{J}}-\sum_{k=1}^{N_b}\Delta m_{bk}\mathbf{r}_{bk}^{\times}\mathbf{r}_{bk}^{\times} \tag{30}$$

where N_b is the number of ballonets, $\mathbf{r}_{bk}$ are the positions of the ballonets, Δm_{bk} are the change of the ballonet masses due to inflation or deflation, $\overline{m}$, $\overline{\mathbf{r}}_G$, and $\overline{\mathbf{J}}$ are the initial mass, position of CG, and inertia tensor of the airship before the ballonets are inflated or deflated. No simulation results are presented in [104] to demonstrate the ballonet influence on airship dynamics.

Mueller et al. [68] incorporated the mass variation of ballonets into the point-mass dynamics model for the ascent trajectory optimization of stratospheric airships. Under neutral buoyancy condition, the total mass of the airship including the ballonets depends on the hull volume as ρV_B, where the air density ρ is a function of the altitude H. Recall that V_B is the total airship volume. Then, Mueller et al. incorporated an additional force due to the air ejection from the ballonets, i.e., [68]

$$F_b=\dot{m}_bV=V_B\frac{\partial\rho}{\partial H}\dot{H}V \tag{31}$$

where m_b is the mass of the ballonet air. Because the altitude changes slowly during the ascent (with an increase of about 20 km in 5 h) in [68], the force F_b is small and has minor influence on the airship dynamics.

Note that the relative motion between the ballonets and the hull is not considered in [104,68]. In the work of Maekawa and Saito [101], the ballonet is assumed to be a cylindrical container and the internal air to be the sloshing fluid in it. With this assumption, the motion of the ballonet sloshing can be analyzed using the dynamics models that have been developed for the sloshing liquids in moving containers [105,106]. As illustrated in Fig. 20(a), the fluid is modeled in two parts: one sloshing in the container (represented by an infinite number of oscillating masses $m_1,m_2,\ldots,m_n$) and one fixed relative to container (represented by a mass m_{b0} and a moment of inertia I_{b0}). The analytical expressions for $m_1,m_2,\ldots,m_n$ can be found in [105,106]. It is found that $m_2,m_3,\ldots,m_n$ are much smaller than m_1, and thus, can be neglected [101]. To incorporate the ballonet sloshing into the longitudinal linear dynamics model, a new differential equation is written to describe the motion of m_1 as [101]

$$\ddot{y}_1+2\zeta_1\omega_1\dot{y}_1+\omega_1^2y_1=-\dot{u}+(h_1-l_{zb})\dot{q}-g\theta \tag{32}$$

where y_1 is the displacement of m_1 from its equilibrium position, ζ_1 is the damping ratio, ω_1 is the undamped natural frequency, h_1 is the vertical position of m_1 from the ballonet CG (see Fig. 20(a)), and l_{zb} is vertical distance between the ballonet CG and the hull CV. The analytical expressions for ω_1 and h_1 can be found in [105,106]. The right hand side of Eq. (32) represents the excitation of the sloshing mass due to the airship motion. Then, the reaction force (in the x direction) and moment (in the y direction) from the ballonet to the airship are incorporated into the linear dynamics model of the airship (the first equation in (11)).

The simulated responses of $\dot{u}$ and $\ddot{y}_1$ to elevator step input (see Fig. 20(b)) are used to evaluate the influence of ballonet sloshing on the rigid-body motion of a 25 m airship [101] with two ballonets. In that study, three cases for the ballonet dimensions are considered. In the first (nominal) case, each ballonet occupies about 6.5% of the envelope volume, the sloshing mass m_1 of each ballonet is about 18% of the ballonet mass m_b, the damping ratio ζ is 0.01, and the sloshing frequency ω_1 is 0.53 Hz, which is approximately five times the airship's longitudinal pendulum frequency (see Section 3.3) of 0.1 Hz. The ballonet slosh has only a minor influence on the airship

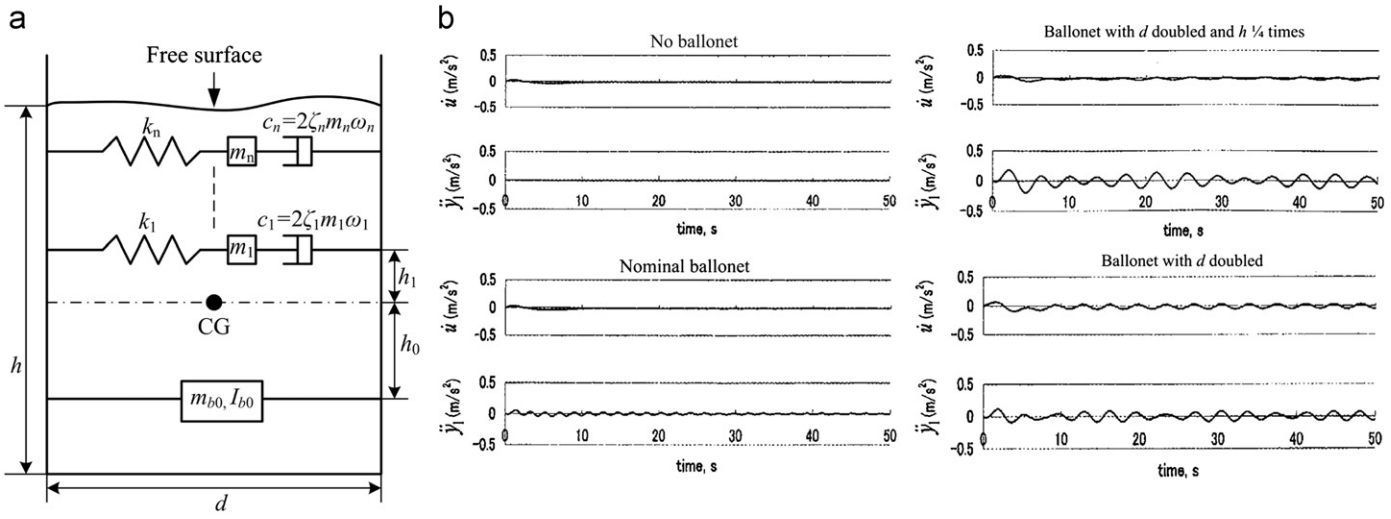

Fig. 20. (a) Ballonet sloshing model and (b) simulation results in [101].

rigid-body motion. If the ballonet shape becomes squatter (with the diameter doubled and the height reduced to 1/4 of the nominal case), the sloshing mass becomes bigger (about 76% of m_b) and the sloshing frequency is reduced to 0.27 Hz. The sloshing vibration exhibits a larger amplitude than that of the nominal case and there is a more noticeable effect on the rigid-body motion. If the ballonet is of the nominal height and twice the diameter (third case), it occupies 53% of the envelope volume. In this case, the sloshing frequency is 0.37 Hz and m_1 is about 36% of m_b, and it is observed that $\dot{u}$ oscillates with the largest amplitude due to the ballonet sloshing. The simulation study in [101] demonstrates that the influence of ballonet sloshing on the airship motion depends on the geometry of the ballonet.

6.3. Semi-empirical models

A semi-empirical method has been applied to investigate the influence of ballonet motions on the longitudinal stability of tethered aerostats [103]. This method accounts for the slosh of ballonet air and lifting gas, both of which are modeled as lumped masses (m_b and m_g) acted on by a spring and a dashpot, as shown in Fig. 21. To incorporate the ballonet motions into the linear dynamics model of the tethered aerostat, a motion equation is derived for m_b as [103]

$$\hat{M}\ddot{x}_b+\hat{C}\dot{x}_b+\hat{K}x_b=-\left(m_b-m_g\frac{V_b}{V_g}\right)\dot{u}-\left(m_b l_{zb}-m_g l_{zg}\frac{V_b}{V_g}\right)\dot{q}-\left(m_b-m_g\frac{V_b}{V_g}\right)g\theta \tag{33}$$

where x_b denotes the displacement of m_b from its equilibrium position, V_b is the volume of ballonet air and V_g is the volume of lifting gas, l_{zb} and l_{zg} are the vertical distances from the hull CV to the CG of the ballonet air and lifting gas, $\hat{M}$, $\hat{C}$, and $\hat{K}$ are an equivalent mass, damping coefficient, and stiffness, respectively. The mass term is $\hat{M}=m_b+m_g(V_b/V_g)^2$ and the stiffness $\hat{K}$ and damping coefficients $\hat{C}$ are determined from experiments, as mentioned in Section 6.1. Then, the reaction forces and moment from the ballonet and the gas are added to the corresponding force and moment terms into the linear dynamics model of the aerostat.

Simulation results for the SN-204 aerostat in [103] show that the ballonet motion has a strong impact on the modes of the tethered aerostat, in particular, the pitching of the aerostat couples with the ballonet slosh. The first mode of the tethered aerostat is a tether-induced pendulum mode and is unchanged by the ballonet. The second mode is related to the pitch rotation and while the damping of this mode is unchanged by the ballonet, its frequency decreases to half of its original value due to the ballonet sloshing. Furthermore, a new third mode is introduced by the ballonet. Although this new mode is stable, its damping ratio is of the same order of magnitude as of the first aerostat mode, which has been considered the least stable and most important mode for design purposes.

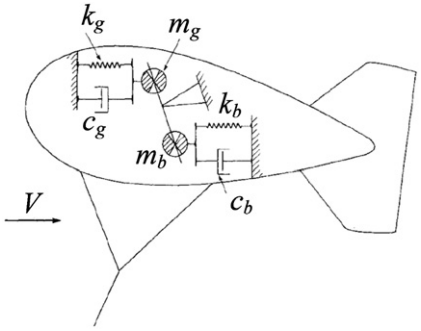

Fig. 21. DeLaurier's model for ballonet sloshing [103].

The modeling method in [101,103] are different in two respects. First, the sloshing motion of the lifting gas is considered in [103] but not in [101]. Second, the estimation methods for the sloshing damping and stiffness terms are different. In [101], the sloshing frequency ω_1 is obtained from the analytical solution for sloshing liquids in containers, and the damping ratio ζ_1 is arbitrarily chosen in the range 0.01–0.1. In [103], the equivalent stiffness $\hat{K}$ and damping coefficient $\hat{C}$ are obtained by employing parameter identification on experimental data.

Different sloshing characteristics of ballonets are obtained in [103,101]. First, the equivalent sloshing mass $\hat{M}$ is larger than the ballonet mass m_b in [103], while the sloshing mass m_1 is only 18% of the ballonet mass in the nominal case in [101]. Second, the undamped natural frequency of the ballonet sloshing in [101] is as high as five times of the airship's longitudinal pendulum frequency, while the natural frequency of the ballonet sloshing is only 1.4 times of aerostat's longitudinal pitch mode frequency in [103]. Finally, the ballonet influence on the aerostat motion is found to be considerable in [103], while this influence is rather small for the airship in [101].

6.4. Summary

To understand the ballonet influence on airship dynamics, two relevant issues have been considered: the variation of mass due to inflation and deflation of ballonets, and the motion of ballonets relative to the hull.

For flight in a large range of altitudes, the volume of ballonet air changes dramatically. Thus, the effects of ballonet mass variation on the total mass matrix of the airship must be considered in the dynamics modeling. On the other hand, if the airship ascent speed is low, the force due to the air ejection from the ballonets can be ignored.

The modeling of the ballonet slosh relative to the hull is a more complicated problem. Spring-mass-dashpot models have been proposed for the ballonet slosh modeling and the induced reaction forces transmitted to the airship have been studied. One difficulty lies in determining the parameters of these spring-mass-dashpot models. Some analytical results available for sloshing liquids in rigid containers can be used to compute the sloshing frequency for a preliminary check against the longitudinal pendulum frequency of the airship. However, their utility is limited, since the ballonet slosh frequency is sensitive to the shape of the ballonet envelope and to how the ballonet and hull envelopes are attached together. A semi-empirical method where the model parameters are identified from experimental data, as in [103], is likely to produce a more accurate model of ballonet sloshing. Generally speaking, the modeling of ballonet sloshing is still not well understood and requires further research supported by experimentation.

7. Conclusions

A state-of-the-art literature review on airship dynamics modeling is presented. The references are categorized according to the major topics in this area: aerodynamics, flight dynamics, incorporation of structural flexibility, incorporation of atmospheric turbulence, and effects of ballonets. Relevant analytical, numerical, and semi-empirical techniques are discussed, pointing out differences between LTA and HTA aircraft.

It should be noted that the five topics addressed in this review are interrelated, as illustrated by the diagram in Fig. 22. Collar suggested to use a triangle of inertial, elastic, and aerodynamic forces to visualize disciplines of flight dynamics, structural

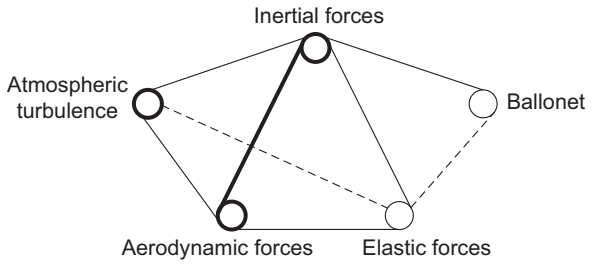

Fig. 22. The interrelation of the five topics.

vibrations, and aeroelasticity [76]. For example, in flight dynamics, one studies the interaction between inertial and aerodynamic forces, and aeroelasticity deals with the interaction between aerodynamic and elastic forces. We have included atmospheric turbulence and ballonet effects into the diagram because of their importance for airship dynamics. The thicknesses of the lines and circles quantify the amount of existing research in each discipline for airships. Many airship dynamics analyses, either experimental or theoretical, are focused on aerodynamics and flight dynamics. Although the construction of modern airships using inflated membrane structures is a major difference from HTA aircraft, research on the coupling between elastic forces and aerodynamic and inertial forces is limited. The modeling of atmospheric turbulence has been studied in detail for the flight dynamics of HTA aircraft. With researchers' recent effort, the methodology to incorporate the turbulent wind into airship aerodynamic and flight dynamic models has been improved. Since atmospheric turbulence can produce a high frequency disturbance on the system, it may excite structural vibrations which in turn may influence the airship's dynamics, and this has not been investigated in the literature. Researchers have demonstrated that the ballonets' motions induce reaction forces and moments on the airship. The ballonets' motion relative to the hull is still difficult to model accurately. If the internal lifting gas pressure is high enough to maintain the hull shape during the flight, it is reasonable to assume that the ballonets have no influence on the aerodynamics. Thus, there are no lines connecting aerodynamic force and ballonets in the diagram in Fig. 22. Existing studies on ballonet motion show that the ballonet sloshing frequency is higher than that of the airship rigid-body modes and may approach the lowest structural vibration frequency, causing an interplay between the two motions. However, no research has been published to date on the interaction of ballonet motion and structural deformations.

This literature review may also be useful for the analysis of unconventional airships, most of which are still only in the conceptual design stage. Other than the hybrid heavy lift airship described in Section 3, few works have been published on the dynamics of unconventional airships. Although existing airship dynamics modeling techniques reviewed in this manuscript may be inadequate for unconventional airships, the review should provide a starting point for further advancement of these methods.

References

[1] Gerken LC. Airships: history and technology. Chula Vista, CA: American Scientific Corporation; 1990. p. 1–19.
[2] Wilson JR. A New era for airships. Aerospace America 2004;42(5):27–31.
[3] Khoury G, Gillett J. Airship technology. Cambridge, UK: Cambridge University Press; 1999. p. 4–17, 28–39, 141–209, 475–504.
[4] Oh S, Kang S, Lee K, Ahn S, Kim E. Flying display: autonomous blimp with real-time visual tracking and image projection. In: Proceedings of the IEEE/RSJ international conference on intelligent robots and systems, Beijing, China, 2006. p. 131–6.
[5] Colozza A, Dolce JL. High-altitude, long-endurance airships for coastal surveillance. NASA TM-2005-213427; 2005.
[6] Dorrington GE. Development of an airship for tropical rain forest canopy exploration. Aeronautical Journal 2005;109:361–72.
[7] Hygounenc E, Jung I, Soueres P, Lacroix S. The autonomous blimp project of LAAS-CNRS: achievements in flight control and terrain mapping. The International Journal of Robotics Research 2004;23(4–5):473–511.
[8] Kulczycki EA, Joshi SS, Hess RA, Elfes A. Towards controller design for autonomous airship using SLC and LQR Methods. In: AIAA Guidance, navigation and control conference and exhibit, Keystone, Colorado, August 21–24, 2006.
[9] Elfes A, Bueno SS, Bergerman M, Paiva ECD, Ramos JG, Azinheira JR. Robotic airships for exploration of planetary bodies with an atmosphere: autonomy challenges. Autonomous Robots 2003;14(2–3):147–64.
[10] Kusagaya T, Kojima H, Fujii HA. Estimation of flyable regions for planetary airships. Journal of Aircraft 2006;43(4):1177–81.
[11] Pope C. The big lift. Professional Engineering 2004;17(8):24–5.
[12] Schmidt DK. Modeling and near-space stationkeeping control of a large high-altitude airship. Journal of Guidance, Control and Dynamics 2007;30(2):540–7.
[13] Lee S, Bang H. Three-dimensional ascent trajectory optimization for stratospheric airship platforms in the jet stream. Journal of Guidance, Control and Dynamics 2007;30(5):1341–52.
[14] Lee Y-G, Kim D-M, Yeom C-H. Development of Korean high altitude platform systems. International Journal of Wireless Information Networks 2006;13(1):31–42.
[15] Etkin B. Dynamics of flight: stability & control. 3rd ed.. New York: Wiley; 1996. p. 93–104, 156–9.
[16] Liao L, Pasternak I. A review of airship structural research and development. Progress in Aerospace Sciences 2009;45(4–5):83–96.
[17] Fossen TI. Guidance and control of ocean vehicles. New York: Wiley; 1998 p. 5–56.
[18] Jones R. The aerodynamical characteristics of the airship as deduced from experiments on models, with application to motion in a horizontal plane. Journal of Royal Aeronautical Society 1924;28(158):88–150.
[19] Curtiss HC, Hazen DC, Putman WF. LTA aerodynamic data revisited. Journal of Aircraft 1976;13(11):835–44.
[20] H.B. Freeman, Force measurements on a 1/40-scale model of the U.S. Airship Akron. NACA TR-432; 1933.
[21] Freeman HB. Pressure distribution measurements on the hull and fins of a 1/40-scale model of the U.S. Airship Akron. NACA TR-443; 1934.
[22] Zahm AF. Air forces, moments and damping on model of fleet airship Shenandoah. NACA TR-215; 1926.
[23] Jones R, Bell AH. Experiments on a model of the airship R.101. ARC RM-1168; 1926.
[24] Jones R, Bell AH. The distribution of pressure over the hull and fins of a model of the rigid airship R.101, and a determination of the hinge moments on the control surfaces. ARC RM-1169; 1926.
[25] Gomes SBB. An investigation into the flight dynamics of airships with application to the YEZ-2A. PhD thesis, Cranfield Institute of Technology; 1990.
[26] Curtiss HC, Hazen DC, Putman WF. Experimental investigations on hull–fin interferences of the LOTTE airship. Aerospace Science and Technology 2003;7(8):603–10.
[27] Jones SP, DeLaurier JD. Aerodynamic estimation techniques for aerostats and airships. Journal of Aircraft 1983;20(2):120–6.
[28] McCormick BW. Aerodynamics, aeronautics and flight mechanics. 2nd ed.. New York: Wiley; 1995. p. 99–116, 160–5.
[29] Munk MM. The aerodynamic forces on airship hulls. NACA TR-184; 1924.
[30] Lamb H. Hydrodynamics. 6th ed.. New York: Dover; 1945. p. 160–201.
[31] Newman JN. Marine hydrodynamics. Cambridge, MA: MIT Press; 1977 p. 132–49.
[32] Lutz T, Fund P, Jakobi A, Wagner S. Summary of aerodynamic studies on the lotte airship. In: Proceeding of the 4th international airship convention and exhibition, Cambridge, UK, July 28–31, 2002.
[33] Blevins RD. Formulas for natural frequency and mode shape. New York: Robert E. Krieger Publishing Company; 1979.
[34] Li Y, Nahon M. Modeling and simulation of airship dynamics. Journal of Guidance, Control and Dynamics 2007;30(6):1691–700.
[35] Thomasson PG. Equations of motion of a vehicle in a moving fluid. Journal of Aircraft 2000;37(4):630–9.
[36] Allen HJ, Perkins EW. Characteristics of flow over inclined bodies of revolution. NACA RM-A50L07; 1951.
[37] Hopkins EJ. A semi-empirical method for calculating the pitching moment of bodies of revolution at low mach numbers. NACA RM-A51C14; 1951.
[38] Hoak DE. USAF stability and control DATCOM. Flight Control Division, Air Force Dynamics Laboratory, Wright-Patterson Air Force Base, OH; 1965 [Section 4.2].
[39] Jorgensen LH. Prediction of static aerodynamic characteristics for space-shuttle-like and other bodies at angles of attack 0° to 180°. NASA TN-D-6996; 1973.
[40] Peddiraju P, Liesk T, Nahon M. Dynamics modeling for an unmanned, unstable, fin-less airship. In: 18th AIAA lighter-than-air technology conference, Seattle, Washington, May 4–7, 2009.
[41] Pitts WC, Nielsen JN, Kaattari GE. Lift and center of pressure of wing-body-tail combinations at subsonic, transonic and supersonic speeds. NACA TR-1307; 1957.
[42] DeLaurier JD. A stability analysis for tethered aerodynamically shaped balloons. Journal of Aircraft 1972;9(9):646–51.

[43] Lambert C, Nahon M. Stability analysis of a tethered aerostat. Journal of Aircraft 2003;40(4):705–15.
[44] Hoerner SF. Fluid-dynamic drag. NJ: Midland Park; 1958. p. 1–19.
[45] Dorrington GE. Drag of spheroid-cone shaped airship. Journal of Aircraft 2006;43(2):363–71.
[46] Jakobi A, Lutz T, Wagner S. Calculation of aerodynamic forces on inclined airship bodies—boundary layer calculation method. In: 3rd international airship convention and exhibition, Friedrichshafen, Germany, July 1–5, 2000.
[47] Lutz T, Funk P, Jakobi A, Wagner S. Aerodynamic investigations on inclined airship bodies. In: 2nd International airship convention and exhibition, Bedford, UK, July 26–28, 1998.
[48] Jakobi A, Funk P, Lutz T, Wagner S. Modelling of airship wakes applying higher order panel elements. In: 14th AIAA lighter-than-air technical committee convention and exhibition, Akron, OH, July 15–19, 2001.
[49] Lutz T, Leinhos D, Jakobi A, Wagner S. Theoretical investigations of the flowfield of airships with a stern propeller. In: Proceedings international airship convention and exhibition, Bedford, UK, July 5–7, 1996.
[50] Lutz T, Funk P, Jakobi A, Wagner S. Calculation of the propulsive efficiency for airships with stern thruster. In: 14th AIAA lighter-than-air technical committee convention and exhibition, Akron, OH, July 15–19, 2001.
[51] Lutz T, Wagner S. Drag reduction and shape optimization of airship bodies. Journal of Aircraft 1998;35(3):345–51.
[52] Nejati V, Matsuuchi K. Aerodynamics design and genetic algorithms for optimization of airship bodies. JSME International Journal. Series B: Fluids and Thermal Engineering 2003;46(4):610–7.
[53] Wang X-L, Shan X-X. Shape optimization of stratosphere airship. Journal of Aircraft 2006;43(1):283–7.
[54] Kale SM, Joshi P, Pant RS. A generic methodology for determination of drag coefficient of an aerostat envelope using CFD. In: 5th AIAA aviation, technology, integration, and operations conference, Arlington, VA, September 26–28, 2005.
[55] Wong KY, ZhiYung L, DeLaurier J. An application of source-panel and vortex methods for aerodynamic solutions of airship configurations. In: 6th AIAA lighter-than-air technology conference, Norfolk, VA, June 26–28, 1985. p. 78–83.
[56] Pannell JR, Bell AH. Experiments on rigid airship R.29. ARC RM-675; 1920.
[57] Thompson FL. Full-scale turning characteristics of the U.S.S. Los Angeles. NACA TR-333; 1930.
[58] Bailey DB. Patrol Airship Concept Evaluation (PACE): Final Report, NADC-85019-60, 1985.
[59] Jex HR, Gelhausen P. Pre- and post-flight-test models versus measured skyship-500 control responses. In: 7th AIAA lighter-than-air technology conference, Monterey, CA, August 17–19, 1987. p. 87–97.
[60] Kornienko A. System identification approach for determining flight dynamical characteristics of an airship from flight data. PhD thesis, University of Stuttgart; August 2006.
[61] Flax AH. Comment on 'A comparison of different forms of dirigible equations of motion'. Journal of Guidance, Dynamics, and Control 1979;2(6):544.
[62] Amann JH. A comparison of a nonlinear flight dynamic simulation of an airship with flight test results. In: 7th AIAA lighter-than-air technology conference, Monterey, CA, August 17–19, 1987. p. 78–86.
[63] Ringland RF, Tischler MB, Jex HR, Emmen RD, Ashkenas IL. Flight dynamics analysis and simulation of heavy lift airships. NACA CR-16647; 1982.
[64] Cook MV, Lipscombe JM, Goineau F. Analysis of the stability modes of the non-rigid airship. The Aeronautical Journal 2000;104(1036):279–90.
[65] Yamasaki T, Goto N. Identification of blimp dynamics via flight tests. Transactions of the Japan Society for Aeronautical and Space Sciences 2003;46(153):195–205.
[66] Li Y. Dynamics Modeling and simulation of flexible airships. PhD thesis, McGill University; 2008.
[67] Bestaoui Y, Hima S. Some insights in path planning of small autonomous blimps. Archives of Control Systems 2001;11(3–4):139–66.
[68] Meuller JB, Zhao YJ, Garrard WL. Optimal ascent trajectories for stratospheric airships using wind energy. Journal of Guidance, Control, and Dynamics 2009;32(4):1232–45.
[69] Miele A. Flight mechanics. Volume 1: theory of flight paths. Addison-Wesley; 1962. p. 42–68.
[70] Slegers N, Brown AX. Comment on 'Three-dimensional ascent trajectory optimization for stratospheric airship platforms in the jet stream'. Journal of Guidance, Control, and Dynamics 2009;32(5):1692–3.
[71] Evans JR, DeLaurier JD. The Shenandoah flies again: a computer simulation. In: AIAA lighter-than-air systems technology conference, Annapolis, MD, July 8–10, 1981. p. 62–73.
[72] Kang W, Suh Y, Woo K, Lee I. Mechanical property characterization of film-fabric laminate for stratospheric airship envelope. Composite Structures 2006;75(1–4):151–5.
[73] Pagitz M, Pellegrino S. Shape optimization of 'Pumpkin' balloons. In: AIAA balloon systems conference, Williamsburg, VA, May 21–24, 2007.
[74] Maekawa S, Yoshino T. Tear propagation of a high-performance airship envelope material. Journal of Aircraft 2008;45(5):1546–53.
[75] Hunt JD. Structural analysis of aerostat flexible structure by the finite element method. Journal of Aircraft 1982;19(9):674–8.
[76] Dowell EHD. A modern course in aeroelasticity. 4th ed.. Dordrecht, Netherlands: Kluwer Academic Publishers; 2005.
[77] Meirovitch L, Tuzcu I. Unified theory for the dynamics and control of maneuvering flexible aircraft. AIAA Journal 2004;42(4):714–27.
[78] Sanswire-Tao-Products-Stratellite™, Retrieved from 〈http://www.sanswiretao.com/product-stratellite.htm〉 on June 30; 2010.
[79] Smith MS, Rainwater EL. Applications of scientific ballooning technology to high altitude airships. In: 3rd AIAA annual aviation technology, integration, and operations technical forum, Denver, CO, November 17–19, 2003.
[80] Bessert N, Frederich O. Nonlinear airship aeroelasticity. Journal of Fluids and Structures 2005;21:731–42.
[81] Burgess CP. Airship design. The Ronald Press Company; 1927. p. 109–52.
[82] Amiryants GA, Grigorive VD, Ishmuratov FZ, Franz A, d'Henin E, Kaempf B. Investigations of airship aeroelasticity. In: 23rd international congress of aerospace sciences, Toronto, Canada, 2002.
[83] Omari K, Schall E, Koobus B, Dervieux A. Inviscid flow calculation around a flexible airship. In: 8th conference of applied mathematics and statistics, Jaca, Spain, September 15–18, 2004.
[84] Liu J-M, Lu C-J, Xue L-P. Investigation of airship aeroelasticity using fluid–structure interaction. Journal of Hydrodynamics 2008;20(2):164–71.
[85] Venkatesan C, Friedmann P. Aeroelastic effects in multi-rotor vehicles with application to a hybrid heavy lift system. Part I: formulation of equations of motion. NASA CR-3822; 1984.
[86] Bennaceur S, Azouz N, Boukraa D. An efficient modelling of flexible airships. In: 8th Biennial ASME conference on engineering systems design and analysis, Torino, Italy, July 4–7, 2006. p. 573–82.
[87] Li Y, Nahon M, Sharf I. Modeling and simulation of flexible airships. AIAA Journal 2009;47(3):592–605.
[88] Vorus WS, Hylarides S. Hydrodynamic added-mass matrix of vibrating ship based on a distribution of hull surface sources. Transactions of the Society of Naval Architects and Marine Engineers 1981;89:397–416.
[89] Kraska M. Structural analysis of the CL-160 airship. In: 14th AIAA lighter-than-air technical committee convention and exhibition, Akron, OH, July 15–19, 2001.
[90] Chen W-J, Xiao W-W, Kroplin B, Kunze A. Structural performance evaluation procedure for large flexible airship of HALE stratospheric platform conception. Journal of Shanghai Jiaotong University 2007;E-12(2):293–300.
[91] Etkin B. Turbulent wind and its effect on flight. UTIAS Review 44, University of Toronto; 1980.
[92] Lagrange MJB. Aerodynamic forces on an airship hull in atmospheric turbulence. Technical Report 277, Institute for Aerospace Studies, University of Toronto; 1984.
[93] Taylor GI. The forces on a body placed in a curved or converging stream of fluid. Proceeding of the Royal Society of London, Series A 1928;120(785):260–83.
[94] Lewis DJG, Lipscombe JM, Thomasson PG. The simulation of remotely operated underwater vehicles. In: ROV'84 conference and exposition, San Diego, CA, 1984. p. 245–51.
[95] Azinheira JR, de Paiva EC, Bueno SS. Influence of wind speed on airship dynamics. Journal of Guidance, Control and Dynamics 2002;25(6):1116–24.
[96] Azinheira JR, de Paiva EC, Bueno SS. Erratum on 'Influence of wind speed on airship dynamics'. Journal of Guidance, Control and Dynamics 2008;31(2):443–4.
[97] Calligeros JM, McDavitt PW. Response and loads on airships due to discrete and random gusts. Technical Report 72-1, Aeroelastic and Structures Research Laboratory, MIT; 1958.
[98] DeLaurier JD, Hui KCK. Airship survivability in atmospheric turbulence. In: AIAA lighter-than-air system technology conference, Annapolis, MD, 1981. p. 48–61.
[99] Layton DM, Wrobleski JJ. The lateral response of an airship to turbulence. In: AIAA lighter-than-air system technology conference, Anaheim, CA, July 25–27, 1983. p. 116–23.
[100] Maekawa S, Nakadate M, Takegaki A. Structures of the low-altitude stationary flight test vehicle. Journal of Aircraft 2007;44(2):662–6.
[101] Maekawa S, Saito K. The effect of ballonet slosh on an airship's longitudinal motion. Transactions of the Japan Society for Aeronautical and Space Sciences 2004;47(155):44–50.
[102] Nakadate M. Development and flight test of SPF-2 low altitude stationary flight test vehicle. In: 5th AIAA aviation, technology, integration, and operations conference, Arlington, VA, September 26–28, 2005.
[103] DeLaurier J. Influence of ballonet motions on the longitudinal stability of tethered aerostats. Journal of Aircraft 1980;17(5):305–12.
[104] Cai Z-L, Qu W-D, Xi Y-G. Dynamic modeling for airship equipped with ballonets and ballast. Applied Mathematics and Mechanics 2005;26(8):1072–82.
[105] Abramson HN. The dynamic behavior of liquids in moving containers with applications to space vehicle technology. NASA SP-106; 1966.
[106] Ibrahim RA. Liquid sloshing dynamics: theory and applications. Cambridge, UK: Cambridge University Press; 2005. p. 296–337.